Tikrit Journal of Pure Science (2023) 28 (5): 74-106
Doi: https://doi.org/10.25130/tjps.v28i5.1584

TJPS

IASJ

المجلات الاكاديمية العراقية

Tikrit Journal of Pure Science
ISSN: 1813 – 1662 (Print) --- E-ISSN: 2415 – 1726 (Online)

Journal Homepage: http://tjps.tu.edu.iq/index.php/j

Geochemical and Economic Assessment of Iron-Rich Bodies in Choman-Rayat Area, Kurdistan Region, Iraq

Zhila Hashim Sadeq[1], Kamal Kolo[1,2] and Mohammad Pirouei[2]
[1]*Scientific Research Center (SRC), Soran University, Soran, Kurdistan Region, Iraq.*
[2]*Department of Petroleum Geoscience, Faculty of Science, Soran University, Soran, Kurdistan Region, Iraq.*

Keywords: Choman-Rayat, Sedimentary iron, Iron-Rich Bodies, Hydrothermal alteration, Bacteriomorphs

ARTICLEINFO.

Article history:

-Received:	**15 July 2023**
-Received in revised form:	**20 Aug. 2023**
-Accepted:	**21 Aug. 2023**
-Final Proofreading:	**24 Oct. 2023**
-Available online:	**25 Oct. 2023**

Corresponding Author*:
Zhila Hashim Sadeq
zhs390h@src.soran.edu.iq

© THIS IS AN OPEN ACCESS ARTICLE UNDER THE CC BY LICENSE
http://creativecommons.org/licenses/by/4.0/

ABSTRACT
This paper reports the finding of potential economic iron mineralization in the ophiolite rocks system in the Choman-Rayat Area, Kurdistan, Iraq. XRD, SEM-EDS, ICP-MS, ICP-OES, and detailed optical microscopy studies indicated that these iron-rich bodies are sedimentary and formed in a hydrothermal alteration system of the abundant serpentinized peridotite in the area with possible microbial interaction. Hematite (up to 55%) is the major mineral in iron-rich bodies, along with quartz, chlorite, and some minor spinel content. In addition to Fe, other potential economic metals associated with iron-rich bodies are nickel (Ni) and cobalt (Co) mineralization. The Ni and Co concentrations ranged from 2094 to 989 ppm and 189.1 to 678.5 ppm respectively. This study adds significant data to the scarcely known or geochemically assessed mineral resources in the Iraqi Kurdistan.

Tikrit Journal of Pure Science (2023) 28 (5): 74-106
Doi: https://doi.org/10.25130/tjps.v28i5.1584

TJPS

الملخص

يشير هذا البحث إلى اكتشاف تمعدن الحديد الاقتصادي المحتمل في نظام صخور الأفيوليت في منطقة جومان رايات، كردستان، العراق. أشارت XRD و-SEM EDS و ICP-MS و ICP-OES ودراسات الفحص المجهري البصري التفصيلي إلى أن هذه الأجسام الغنية بالحديد رسوبية وتشكلت في نظام تغيير حراري مائي للبريدوتيت السربنتيني الوفير في المنطقة مع احتمال التفاعل الميكروبي. الهيماتيت (تصل إلى ٥٥٪) هو المعدن الرئيسي في الأجسام الغنية بالحديد، إلى جانب الكوارتز والكلوريت وبعض محتوى الإسبنيل الطفيف. بالإضافة إلى الحديد، فإن المعادن الاقتصادية المحتملة الأخرى المرتبطة بالأجسام الغنية بالحديد هي تمعدن النيكل (Ni) والكوبالت (Co). تراوحت تركيزات Ni و Co من ٢٠٩٤ إلى ٩٨٩ جزء في المليون و ١٨٩.١ إلى ٦٧٨.٥ جزء في المليون على التوالي. تضيف هذه الدراسة بيانات مهمة إلى الموارد المعدنية النادرة أو المقيمة جيوكيميائيا في كردستان العراق.

1. Introduction:

Mineral exploration in Iraq is relatively young and can be traced back to the second half of the last century, when most of the exploration work was carried out by pioneering geologists [1; 2; 3]. The Kurdistan Region of Iraq, in addition to its important hydrocarbon reserves, is also rich in metallic and non-metallic mineral deposits that are associated with sedimentary rocks, as well as metamorphic and igneous rocks, and many of which are products of hydrothermal processes [4; 5; 6; 7]. These mineral deposits are still not fully studied or economically evaluated. Recently, the Ministry of Natural Resources (MNR) published the first compilation geological study of all known mineral occurrences in Kurdistan based on previously published reports. That study divided Kurdistan into seven blocks with geologic maps and mineral occurrences within each block [8]. The present study area is located within Block 4 (Fig.1). The metallic and nonmetallic mineral occurrences are reported as gold (Au), pyrite (FeS_2), copper (Cu), chromite (Cr), nickel (Ni), manganese (Mn), iron (Fe), and quartz (Qz). Most of these occurrences are reported within the present Rayat area. From those mineral shows, only iron ore deposits were studied in detail in neighboring localities [9]. An early study by Etabi [10] considered Kurdistan's iron accumulation as minor and formed by contact-metasomatic, magmatic, or sedimentary processes. Other researches [6; 11] suggested that the majority of magnetite-hematite occurrences are associated with contact metasomatic processes in the Suture Zone from the Shalair and Walash Groups, whereas the majority of the pyrite and siderite represent low-temperature hydrothermal deposits (along with their oxidation products) were discovered in the Imbricate Zone in the Ora District, specifically in the Kurra Chine, Chia Zairi, and Aqra-Bekhme formations (add references).

Recent study by Pirouei [9] showed important iron ore deposits in the Rayat area resulted from serpentinization processes, followed by the formation of gossanite-type magnetite and hematite with microbial activity mediation and associated with minor mineralizations of sulfide in the Zagros ophiolites. Rayat iron ore is now mined as an open quarry.

This study will present assessment of potential iron and other metal mineralizations in a newly discovered section of the Choman-Rayat area through a combination of fieldwork observations, geochemistry and optical microscopy petrography studies to determine major and trace element concentrations, distributions, and their petrographic associations.

Tikrit Journal of Pure Science (2023) 28 (5): 74-106
Doi: https://doi.org/10.25130/tjps.v28i5.1584

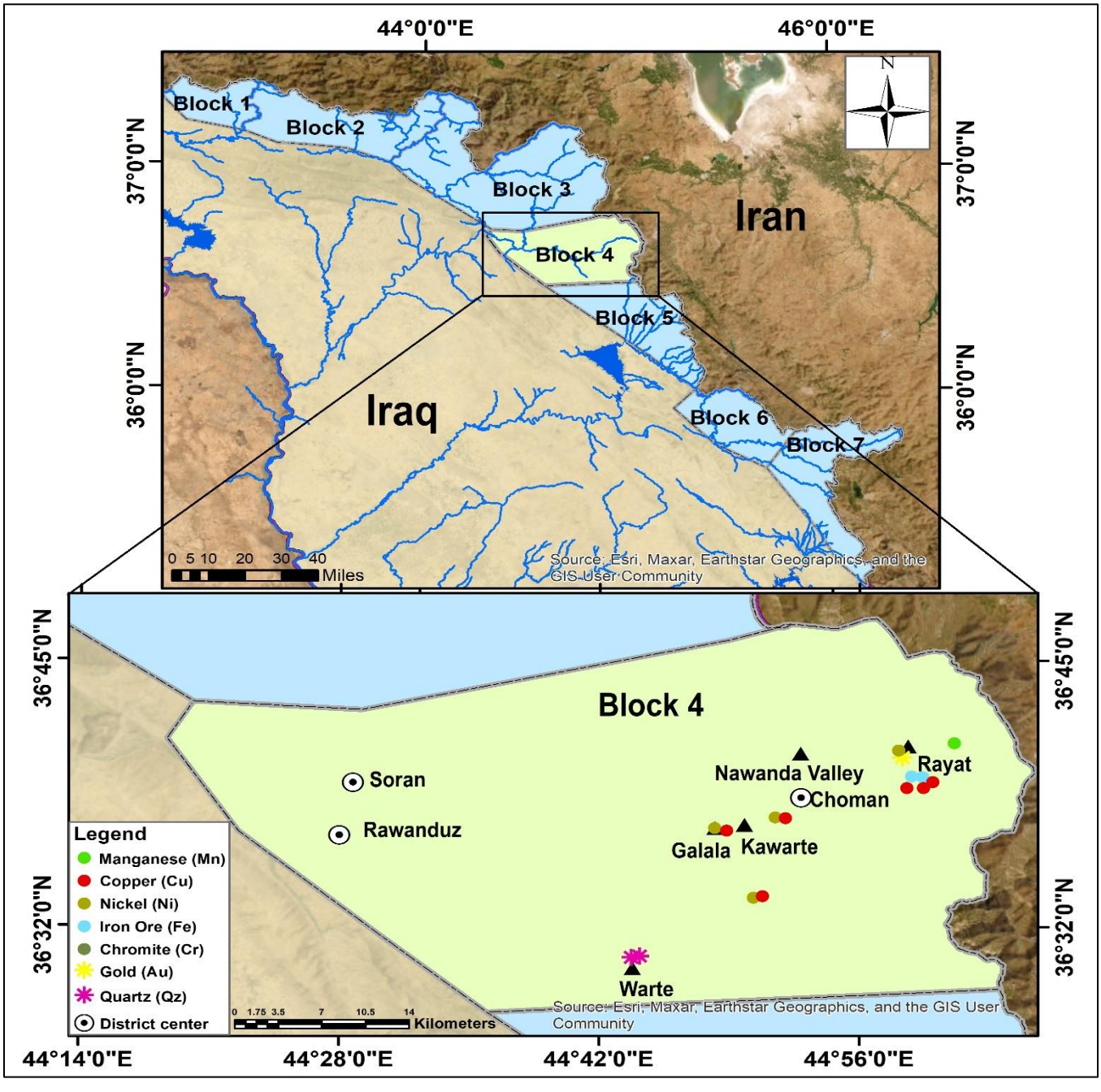

Figure 1: Mineral shows and occurrences map as determined by the MNR study in Block 4 where the present study is located [8].

2. Geology of Study Area

The Choman-Rayat study area is not far from the Iraqi-Iranian border in Iraq's northeastern corner (Fig.2). The area's exposed rocks are part of Alpine-Himalayan Mountain Range System of Iraqi Zagros Suture Zone (IZSZ) (Fig.2a and b) [12; 13; 14]. The Shalair, Penjween-Walash, and Qulqula-Khwakurk subzones are the three tectonic subzones that constitute the IZSZ (Fig.2b).

Geologically, different lithostratigraphic units are represented in the study area, which is

Tikrit Journal of Pure Science (2023) 28 (5): 74-106
Doi: https://doi.org/10.25130/tjps.v28i5.1584

defined by Paleocene-Upper Eocene rock outcrops and includes all the Walash Series parts (Fig.3). Quaternary sediments, primarily as talus and terrace deposits, cover a part of the Walash Group rocks [3]. Sedimentary, volcano-sedimentary, and intrusive rocks constitute the majority of the Walash Group rock types that are exposed in the great Rayat area; the latter rock types mostly consist of listvenites and serpentinized peridotites [15]. Generally, besides the Quaternary sediments and the intrusive rocks, the Rayat area includes three sedimentary rock groups (Fig.3) [3]:

1. The upper (calcareous-argillite) rock group contains massive grey limestones and argillites, conglomerates, sandstone, red siliceous-jasper rocks.
2. The volcanosedimentary rock group (middle group) contains conglomerates, breccia, basalts, sandstones, greywackes, limestones, and dolomites.
3. The lower rock group includes shales, calcareous conglomerates, aphanitic limestones, and marls.

Intrusive rocks can also be found as sheets and sills of changed ultramafic rock. Serpentines constitute most of the metamorphosed intrusive rocks. Aphanitic and granular serpentinites, formed during the alteration of autometasomatic ultrabasic rocks, are the most common types of serpentinized rocks and comprise most of the massive rock exposures. Chromite veins and lenses are primarily found in sheared serpentinites. Talus and terrace deposits constitute most Quaternary sediments [3].

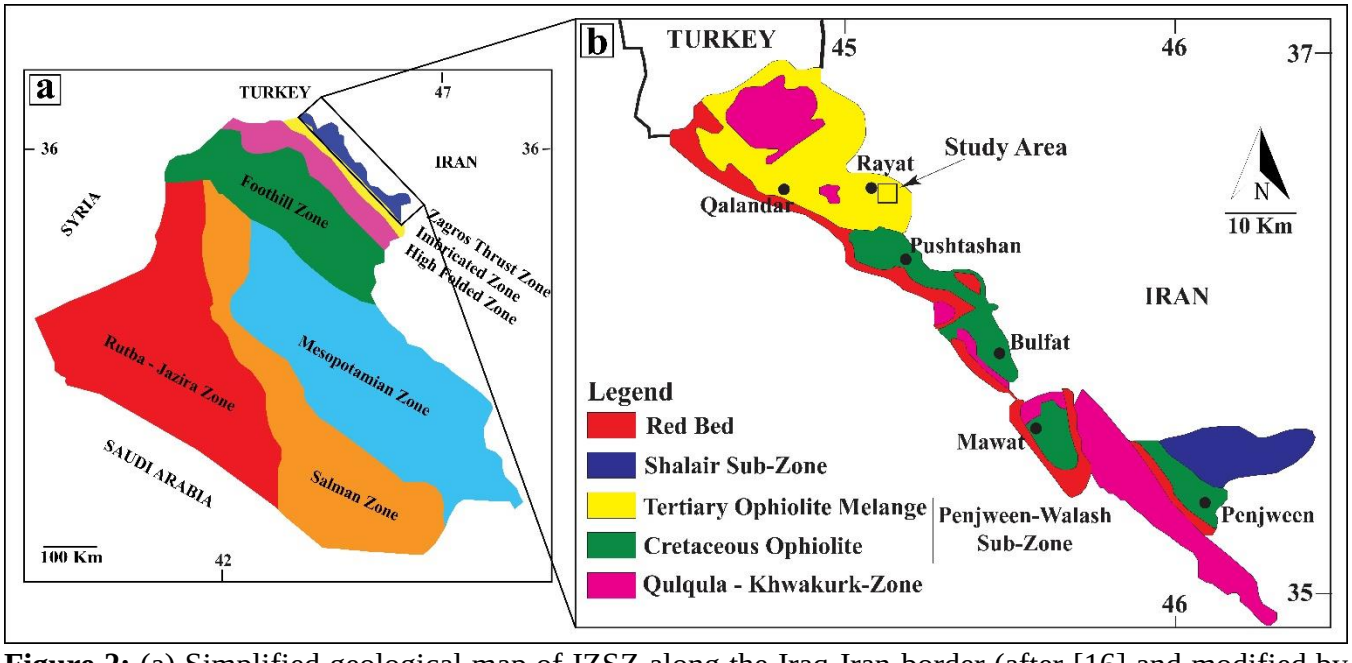

Figure 2: (a) Simplified geological map of IZSZ along the Iraq-Iran border (after [16] and modified by [17]), (b) the broader study area geological map in NE Iraq (modified by [17]).

Tikrit Journal of Pure Science (2023) 28 (5): 74-106
Doi: https://doi.org/10.25130/tjps.v28i5.1584

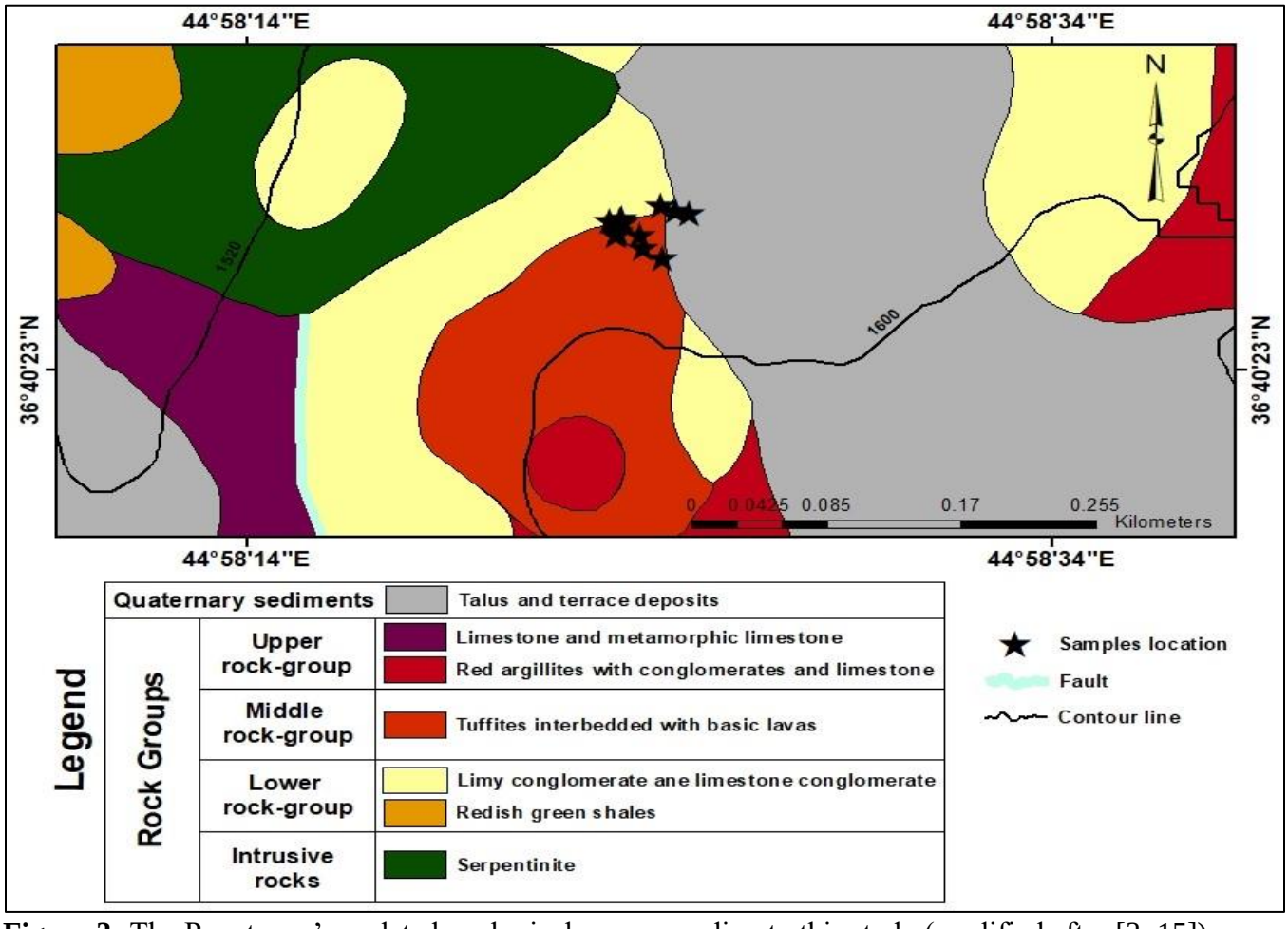

Figure 3: The Rayat area's updated geological map according to this study (modified after [3; 15]).

3. Materials and Methods:

3.1. Sampling:

Several field trips were conducted in the area to record field observations and collect samples. During field trips, the area's detailed geological mapping was conducted, and 41 rock samples were collected from four iron-rich bodies and the surrounding rocks' outcrops for detailed petrographic, mineralogical, and geochemical studies. In the field, all the samples were coordinated by GPS and then numbered and described. Sampling was performed to prepare thin-polished sections and grind them for chemical analyses.

3.2. Petrographic Studies:

A LEICA DM4500P polarized optical microscope was used to study thirty-two polished thin sections from different lithologies containing iron-rich bodies and surrounding rocks. The petrographic analysis of polished thin sections included the detection **of mineral** identifications, fossils, and bioclasts, the identification of diagenetic and texture properties, and the determination of representative interest points for SEM-EDS analysis.

The SEM-EDS analysis was conducted on gold-coated thin-polished sections. At the Scientific Research Center of Soran University in Iraq, an FEI 480 and a BRUKER-QUANTAX energy dispersive X-ray spectrometer were used. The instrument's analytical conditions were as follows: an accelerating voltage of 15-25 kV, a beam current of 20 nA, a beam size of 1-2 m, and a count time of 25 s.

3.3. Mineralogical Determinations:

A PANalytical X-ray diffraction (XRD) analysis was conducted to identify the minerals at the facilities of the Scientific Research Center of Soran University, Iraq. The following were the scanning criteria: Utilizing an X'Celerator detector, 2 = 6-85° with steps of 0.017° and 50 s.

Tikrit Journal of Pure Science (2023) 28 (5): 74-106
Doi: https://doi.org/10.25130/tjps.v28i5.1584

3.4. Geochemical Analyses:

Whole-rock geochemical analysis was done at Zarazma Laboratory in Iran on powdered samples for major and minor elements using Induced Coupled Plasma (ICP-OES) for major elements and ICP-MS for minor and trace elements by fusing the sample with lithium borate before dissolving it in acid.

4. Results:

4.1. Field Observations:

The four iron-rich outcrops are situated in the Rayat area SW (Fig.4). A composite litho-stratigraphic succession of the exposed **deposits** (Fig.5) shows that the iron-rich bodies are generally overlain by calcareous sandstones and shales and bounded by serpentinites (Figs.4a, b, and c). The exposed section of the Fe-enriched body shows a transition zone (TZ) between the iron-rich bodies (IRBs) and calcareous sandstone (CSd) (Fig.5). It is important to note that the transition zone has a brecciated texture with serpentinite, quartz, and chert of various sizes (Fig. 6a and b). Moreover, adjacent to calcareous sandstone, shale can be observed (Figs. 4a and 6a).

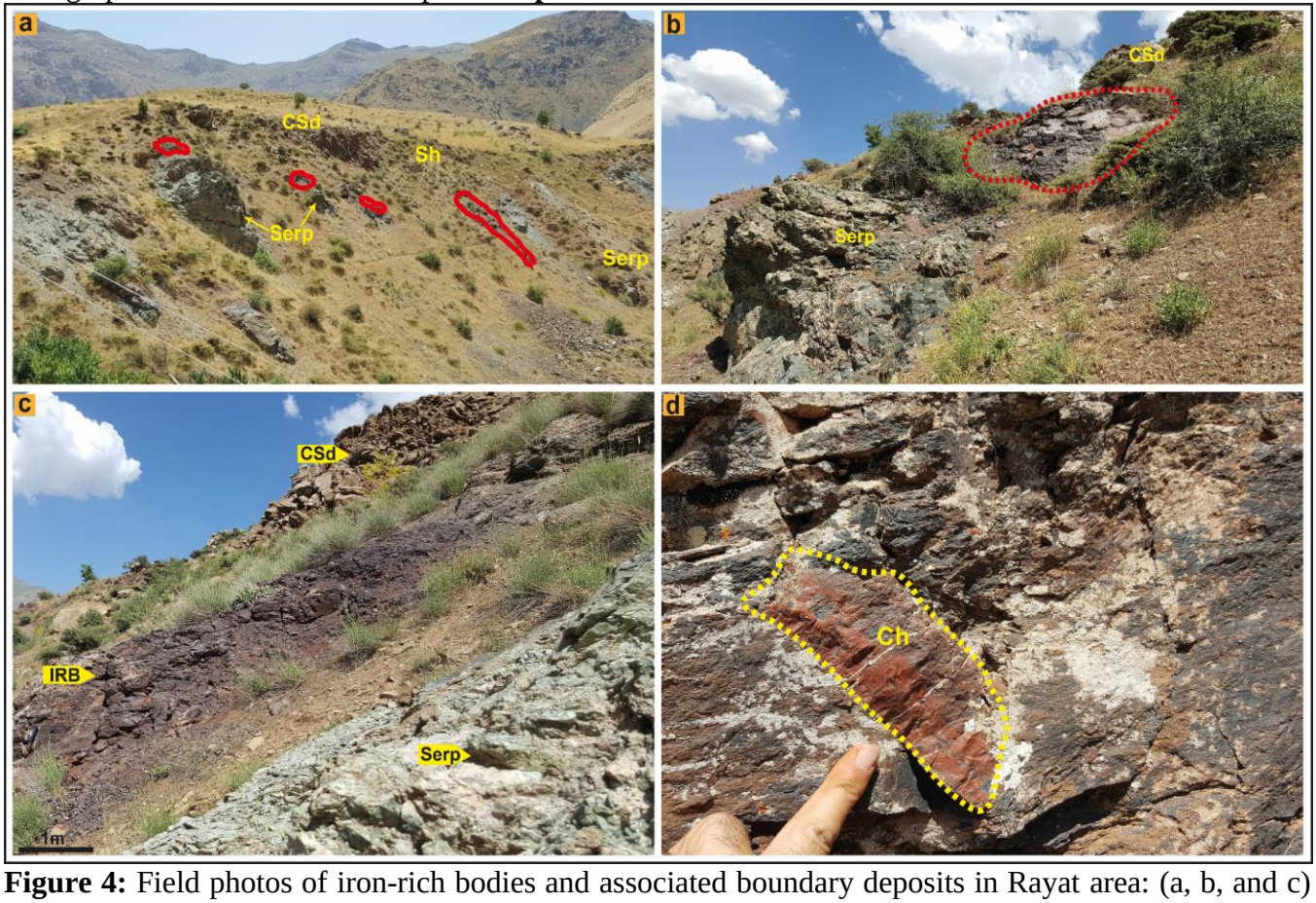

Figure 4: Field photos of iron-rich bodies and associated boundary deposits in Rayat area: (a, b, and c) overview of the iron bodies (red circles in a, and dashed circle in b) and the associated rocks; (d) occurrence of chert clast (jasper) with red-brown color inside iron bodies with different size which is rich in quartz and hematite; (Ch: chert, CSd: calcareous sandstone, IRB: iron-rich body, Sh: shale, Serp: serpentinite).

Tikrit Journal of Pure Science (2023) 28 (5): 74-106
Doi: https://doi.org/10.25130/tjps.v28i5.1584

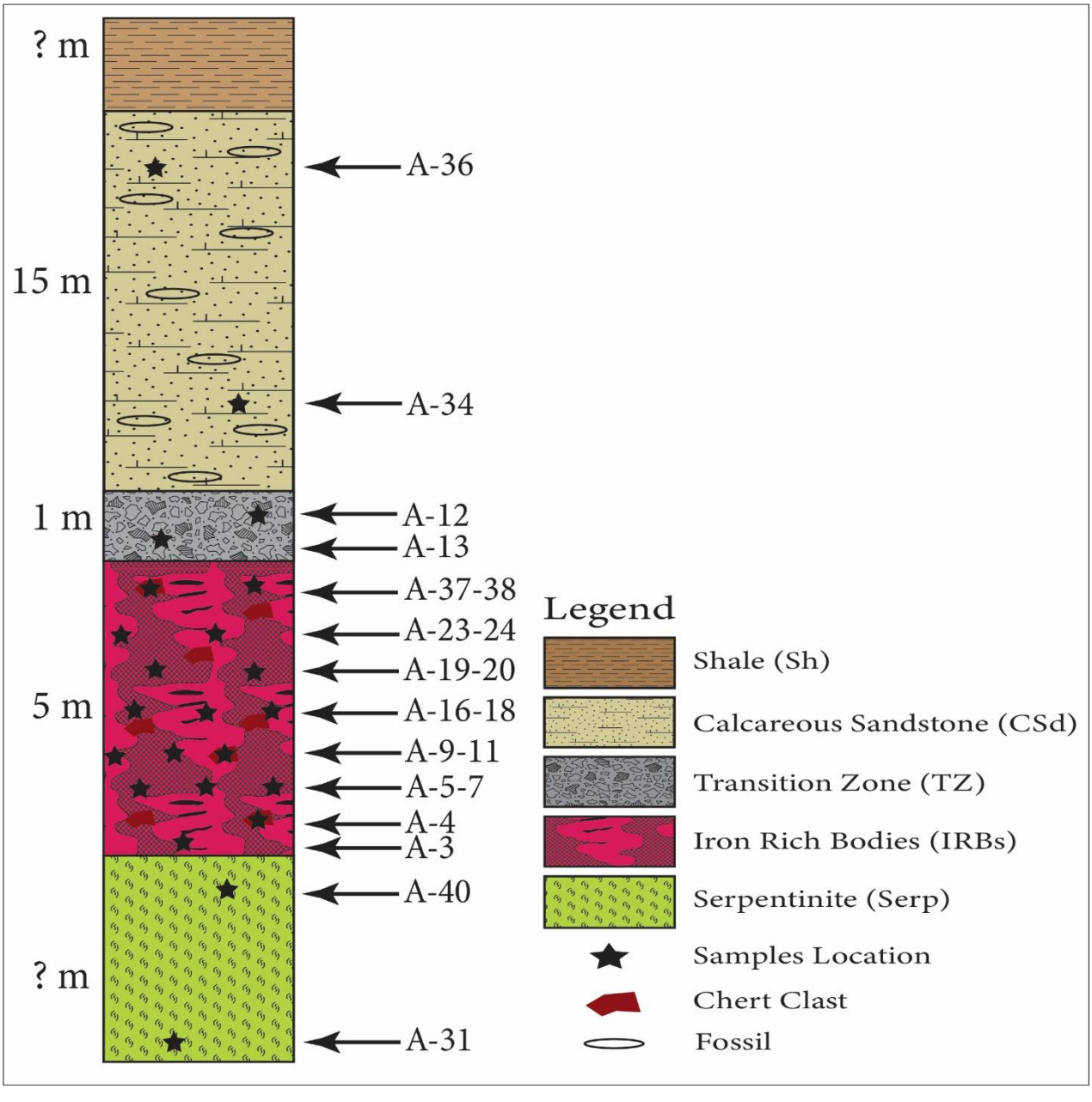

Figure 5: Composite litho-stratigraphic column of the outcrop sections showing the position and thickness of the iron- rich bodies (IRBs) and the associated rocks in Choman-Rayat area.

4.1.1 Deposits Description:

4.1.1.1 Iron-Rich Bodies (IRBs):

The reddish iron-rich bodies are developed between the serpentinites and transition zone (Figs. 4a-c and 5). The iron-rich bodies contain small to coarse particles of quartz and different generations of quartz veins (Fig.7a–f). Due to tectonic and different hydrothermal activities, the veins show bending and cross-cutting features (Fig.7b–e). The mapped **exposed thicknesses of** the iron-rich bodies range between 2 m and 5 m.

4.1.1.2. Chert (Ch):

Clasts of iron-colored reddish chert (Jasper) ranging in size from millimeters to centimeters can be observed inside the iron-rich bodies and transition zone (Figs. 4d, 5, and 6b). Additionally, the chert clasts contain hematite and quartz (Fig.7g).

Tikrit Journal of Pure Science (2023) 28 (5): 74-106
Doi: https://doi.org/10.25130/tjps.v28i5.1584

4.1.1.3. Transition Zone (TZ):
This grainy zone is developed between the iron-rich bodies (IRBs) and calcareous sandstone (CSd) (Fig.5). This zone represents ferruginous? and brecciated texture, containing clasts of different sizes ranging from millimeters to centimeters (Fig.6b). In the hand samples, the transition zone contains some grains composed of iron oxides (Fig.7h).

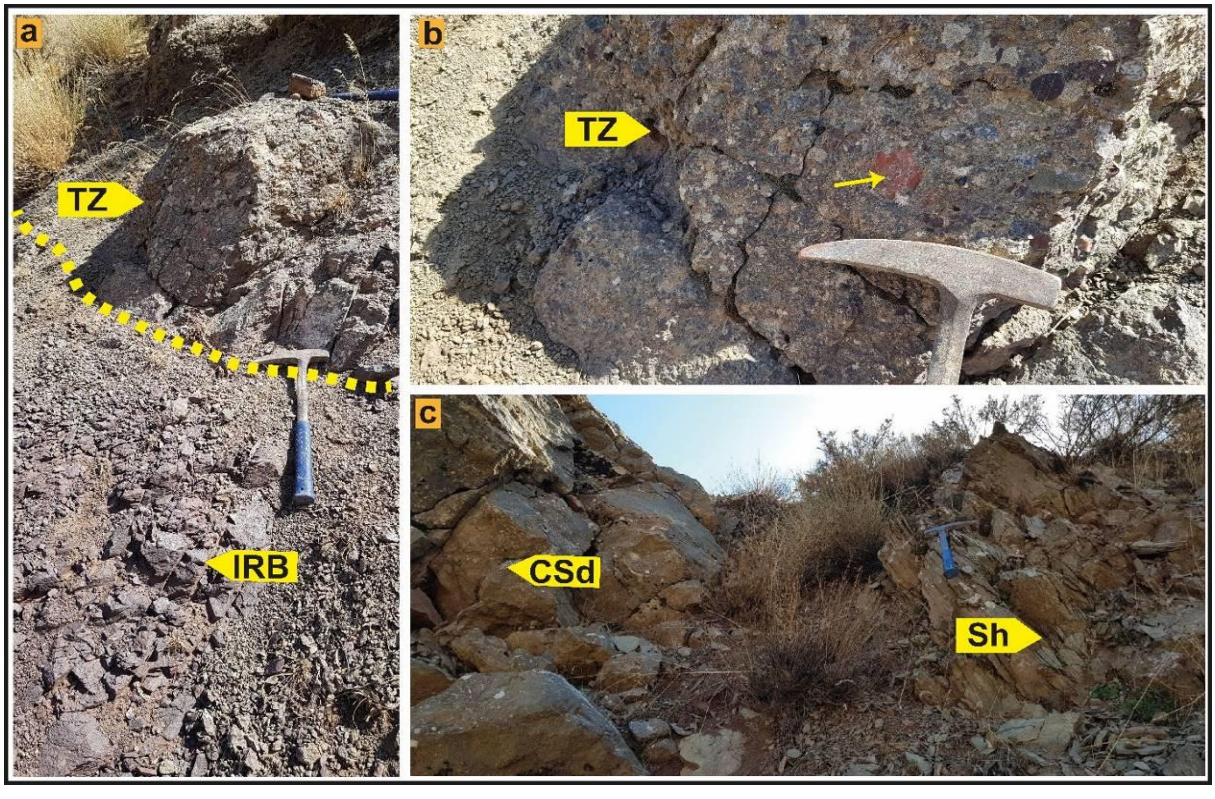

Figure 6: Field photos of iron-rich bodies and associated rocks in Rayat: (a) contact of IRBs with transition zone; The transition zone is grainier and contains less amount of iron minerals; (b) a closer view of TZ which shows the presence of different types of clasts such as ferruginous chert (yellow arrow); (c) contact between calcareous sandstone and shale; (CSd: calcareous sandstone, IRB: iron-rich bodies, Sh: shale, TZ: transition zone).

4.1.1.4. Calcareous Sandstone (CSd):
These whitish-grey, massive, and highly fractured calcareous sandstone deposits overlie the iron-rich bodies (Figs. 4a–c and 6c); they reach thicknesses of up to 15 m. They exhibit a granular texture ranging from fine to medium-grained with visible broken and mixed sizes of clasts of quartz and skeletal fossils bioclasts suggesting a rapid high energy turbulent transport and sedimentation (Fig.7i and j).

4.1.1.5. Serpentinite (Serp):
The light-dark greenish serpentinites are widely prolific in the area and are particularly associated with iron-rich bodies (Fig.4a, b, and c). Moreover, talc veins crosscut the entire mass, and this rock shows different colors (Fig.7k and l).

Tikrit Journal of Pure Science (2023) 28 (5): 74-106
Doi: https://doi.org/10.25130/tjps.v28i5.1584

TJPS

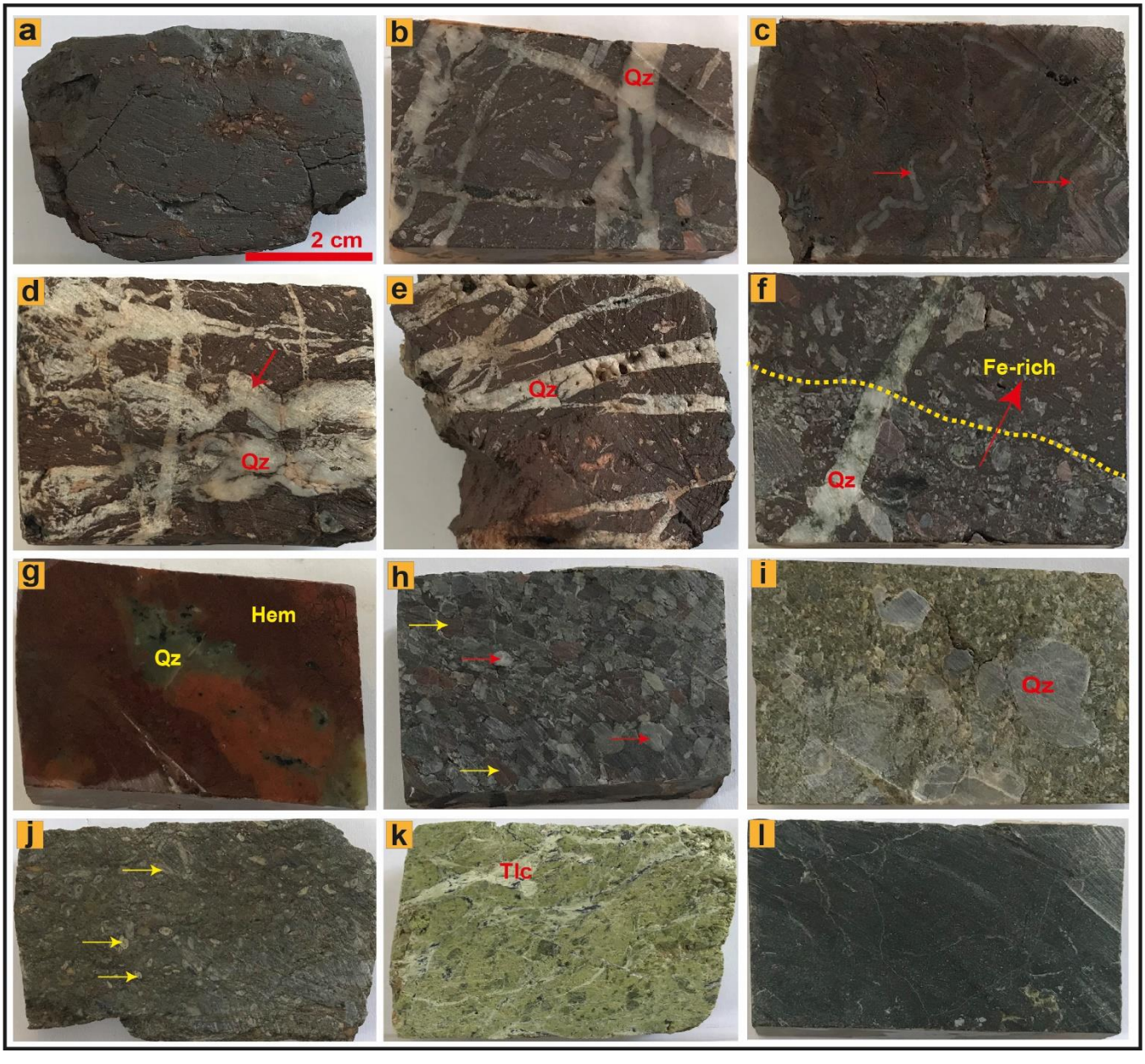

Figure 7: Hand samples of iron-rich bodies and associated rocks in Rayat: (a) samples of iron-rich bodies contain small particles of quartz (b, c, d, and e). The IRBs samples contain small to coarse particles of quartz (whitish spots) and different generations of quartz veins. Occasionally, veins sometimes show bending features due to tectonic stress (red arrows in figs. c and d). The visible vein crosscutting is attributed to hydrothermal activities and probable hydro-fracturing; (f) the transition zone between IRBs and calcareous sandstone, the TZ is grainier. (g) chert sample containing hematite and quartz; (h) transition zone more away from IRBs showing lack or less presence of iron oxides; (i) calcareous sandstone contains clasts of quartz; (j) calcareous sandstone with greenish color containing a high number of fossils (yellowish arrows); (k and l) serpentinite of the area with different colors; (Hem: hematite, Qz: quartz and Tlc; talc).

4.2. Mineralogy and Petrography:

In order to study the petrographic properties, the polished thin sections were studied by optical microscope. During the study petrographic characteristics such as texture, shape, grain size, paragenesis and other properties were determined

Tikrit Journal of Pure Science (2023) 28 (5): 74-106
Doi: https://doi.org/10.25130/tjps.v28i5.1584

TJPS

4.2.1. Iron-Rich Bodies (IRBs):

Based on the mineralogical study and paragenetic sequence that show the mineralization stages of the iron-rich bodies, the iron-rich bodies are rich in hematite, chlorite, and quartz, with minor minerals such as chromite, magnetite, apatite, calcite, and talc (Table 1 and Fig.8). Hematite is an abundant matrix mineral in iron-rich-bodies (Fig.9a, b, and c). In banded hematite chert, hematite is characterized by alternating wavy micro-layers with chert (Fig.9a); these microlayers are indication of changes in the sedimentary environment and hydrothermal fluid composition, and this alternation is noted as an analogy of banded iron formations. Hematite and spinel grains are variable in various shapes and sizes, from rounded to subhedral; hematite is formed as a single subhedral grain, while quartz grains are variable in size and morphology (Fig.9b). Chlorite fills the fractures in between the minerals as well as inside them (Fig.9c). Calcite veins crosscut all other minerals (Fig.9d). The presence of spherical magnetite grains indicates fragmentation, transportation, and probable reworking from an earlier external source (Fig.9e). Apatite is another minor mineral that forms inside the dissolved quartz grains (Fig.9f). Silica occurs as quartz and chert; they are observed as replacing the remains of red algae and foram fossils (Fig.10a–f). Mineralized fossils in most cases show sinuosity structures (Fig.10a and b) and internal wall and cellular segmented structures (Fig.10a, b, d, and f). Due to advanced diagenesis, the foraminifera (nummulite) is completely mineralized (Fig.10c). A multilayer hematite-silicate plate (Fig.10d and e) is enveloped by algal remnants. In most samples, quartz was recrystallized from chalcedony (Fig.10f).

Table 1: Semi quantitative XRD results of the iron-rich bodies and the associated rocks (M: major, m: minor, T: trace).

Sample no.	Lith[1]	Minerals[2]													
		Ap	Cal	Chl	Ctl	Fsp	Hem	Liz	Mag	Pyl	Px	Qz	Spl	Srd	Tlc
A-31	Serp		M		M			M	m		m		T		
A-3	IRB	T		m			T		T			M	m		
A-7	IRB			M			m		T			M	T		
A-16	IRB		m	m			T					M	T		m
A-19	IRB			m		M	m		T			m			
A-23	IRB			m			m					M	T		T
A-9	Chert	m	T	T			T			T		m	T	M	
A-38	Chert		T			m	T					M			
A-13	TZ			m		M	T					m	T		
A-34	CSd		T	T		M						m			

[1] Lithology: Serp: serpentinite, IRB: iron-rich body, TZ: transition zone, CSd: calcareous sandstone

[2] Minerals: Ap: apatite, Cal: calcite, Chl: chlorite, Ctl: chrysotile, Fsp: feldspar, Hem: hematite, Liz: lizardite, Mag: magnetite, Pyl: pyrolusite, Px: pyroxene, Qz: quartz, Spl: spinel, Srd: serandite, Tlc: talc

Tikrit Journal of Pure Science (2023) 28 (5): 74-106
Doi: https://doi.org/10.25130/tjps.v28i5.1584
TJPS

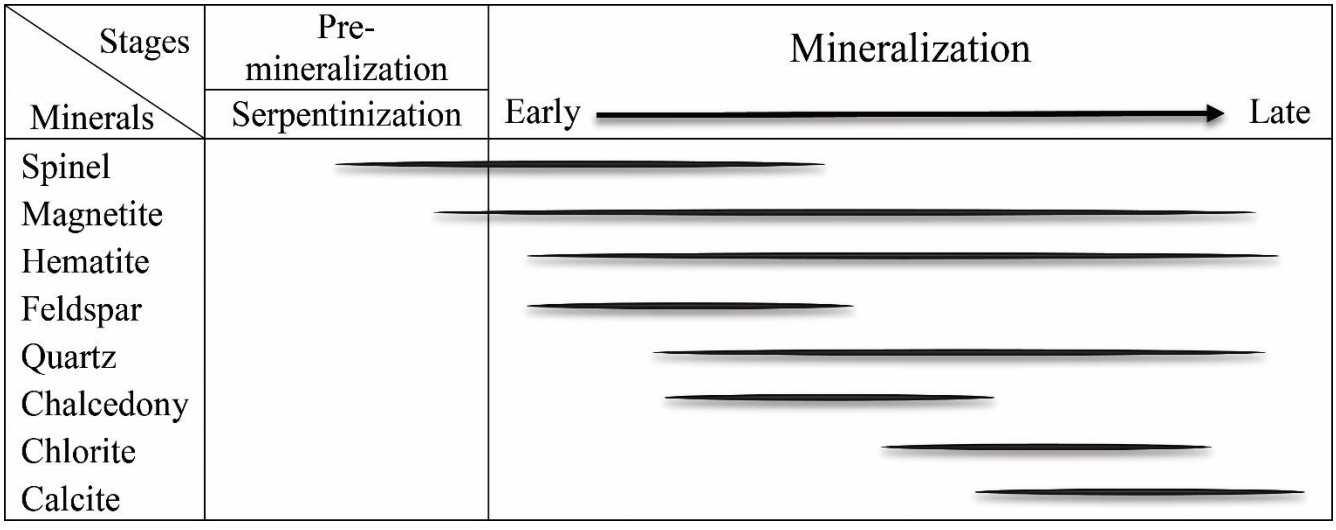

Figure 8: Stages of mineralization and the paragenetic sequence of minerals in the iron-rich bodies.

Tikrit Journal of Pure Science (2023) 28 (5): 74-106
Doi: https://doi.org/10.25130/tjps.v28i5.1584

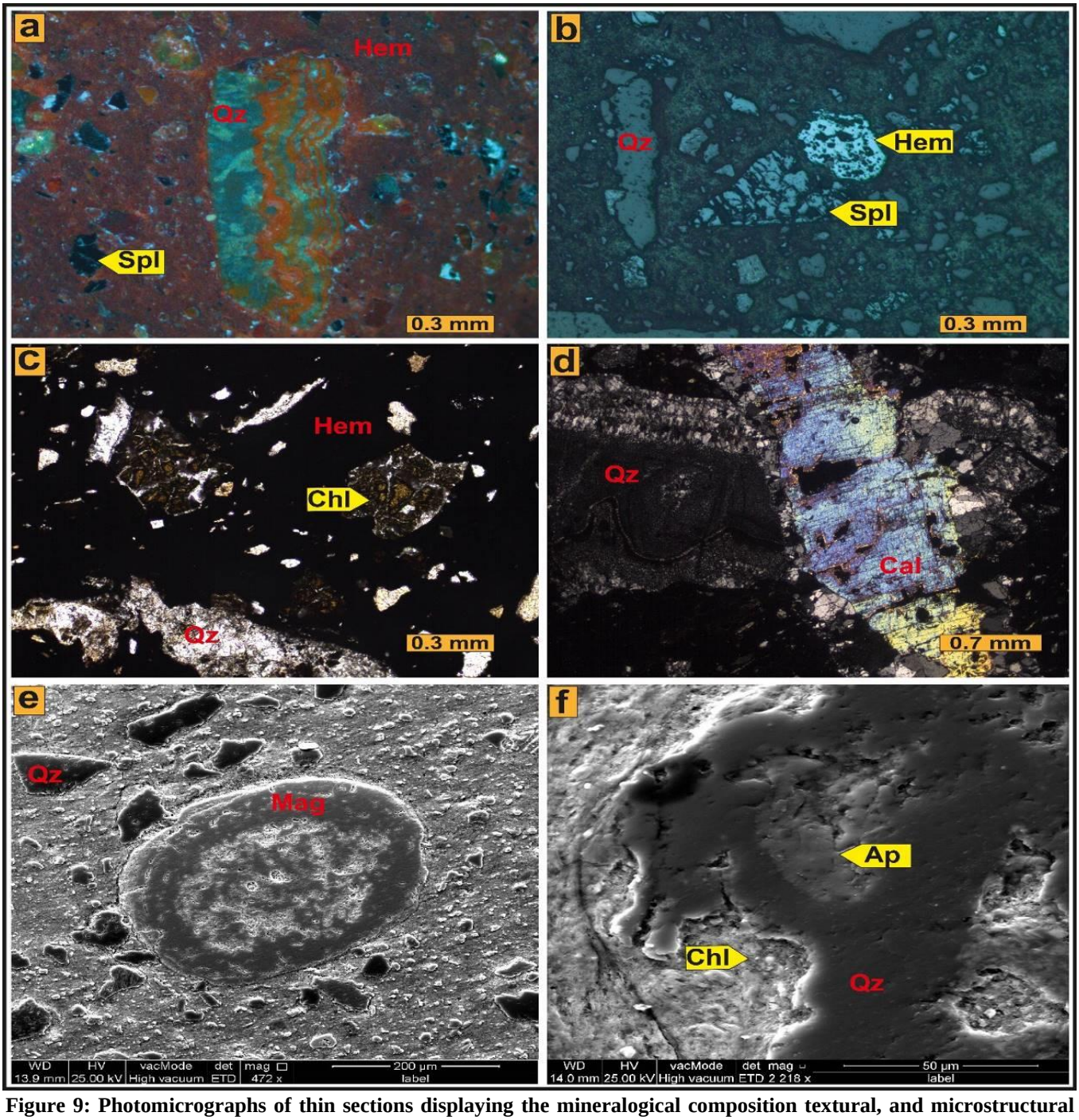

Figure 9: Photomicrographs of thin sections displaying the mineralogical composition textural, and microstructural properties of iron-rich bodies: (a, b, and c) Hematite minerals form the matrix with orange color. Occasionally, the hematite and chert form alternate wavy micro-layers (a), an indication of changes in the sedimentary environment and hydrothermal fluids composition. These microlayers by analogy are a reminder of the similar alternations in Banded Iron Formations. The iron-bearing fragment is reworked and transported from a formerly formed layer. In many instances, the hematite is formed as single grains, whereas, spinels are disseminated in sample of various sizes. Quartz grains are variable in size and morphologies; chlorite is filling the fractures in-between the minerals as well as inside them; (d) shows calcite veins cross-cutting all other mineral phases indicating the last formation phase; (e) the single roundish magnetite grains indicate fragmentation, transportation, and probably reworking from an earlier external

source; (f) apatite mineral formation inside quartz; (Ap: apatite, Chl: chlorite, Hem: hematite, Mag: magnetite, Qz: quartz, Cal: calcite, and Spl: spinel).

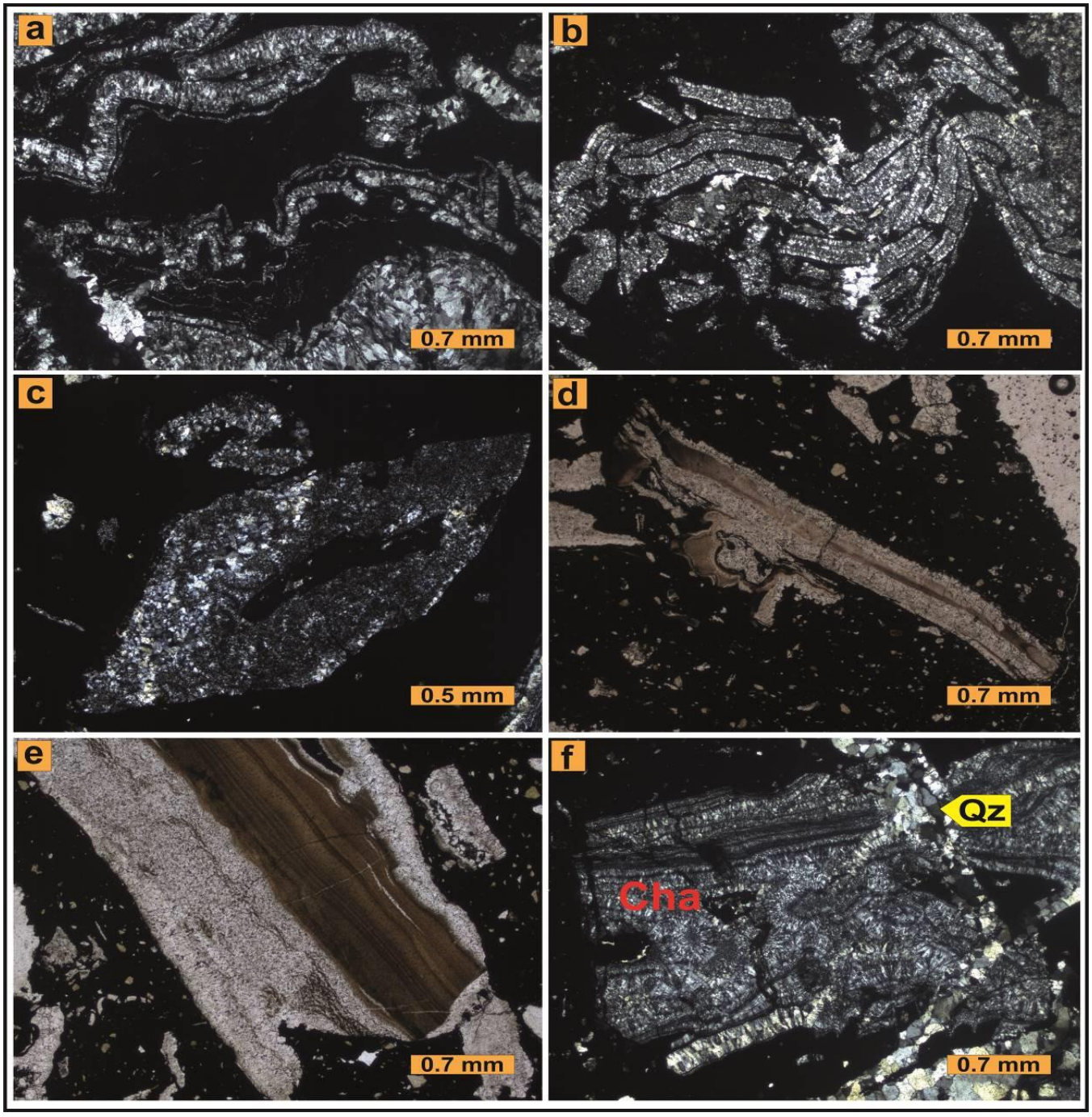

Figure 10: Photomicrographs of thin sections displaying highly mineralized fossil red algae remains and foraminifera, a, b, d, e, f. The structure show sinuosity (a, b), internal wall and cellular segmented structures (a, b, d, f), and a probable cystocarp budding structure (d). Fig.c is typically a nummulite foram that is mineralized and the internal structure is barely visible due to advanced diagenesis; (e) shows a special case where the algal remains envelope a multilayer hematite-silicate plate; (Cha: chalcedony and Qz: quartz).

4.2.2. Chert (Ch):

Cherts are generally found as fragments of different sizes that are ferrugenized and mineralized. According to the optical microscopy, XRD results, and SEM images, the cherts are characterized by quartz, pyrolusite, and serandite with a minor amount of hematite, feldspar, apatite, chlorite, chromite, and calcite (Fig.11a–f; Table 1). The quartz occurs as very fine-grained masses, single crystals, and veins (Fig.11a–c). Muscovite appears as elongated crystals filling the fractures (Fig.11a). Feldspars occurred as veins while calcite veins crosscut the feldspar veins (Fig.11b). Hematite fills fractures and inter-spaces between minerals (Fig.11c). Pyrolusite fillsthe places where fine-grained chert is dissolved and in some cases apatite is formed as an association with pyrolusite (Fig.11d and e). The chlorite fills fractures between the silicate minerals and displays a flaky texture (Fig.11f).

4.2.3. Transition Zone (TZ):

In TZ, feldspar and quartz are the major minerals. Minor minerals include spinel and chlorite (Fig.11g, h, and i). The feldspars are enveloped and crosscut later by quartz veins and have anhedral shapes (Fig.11g and h); however, in most parts, they are altered and replaced by quartz (Fig.11h). Spinel grains in the transition zone show altered boundaries, pitting, and microporosity on the surface (Fig.11i).

Tikrit Journal of Pure Science (2023) 28 (5): 74-106
Doi: https://doi.org/10.25130/tjps.v28i5.1584

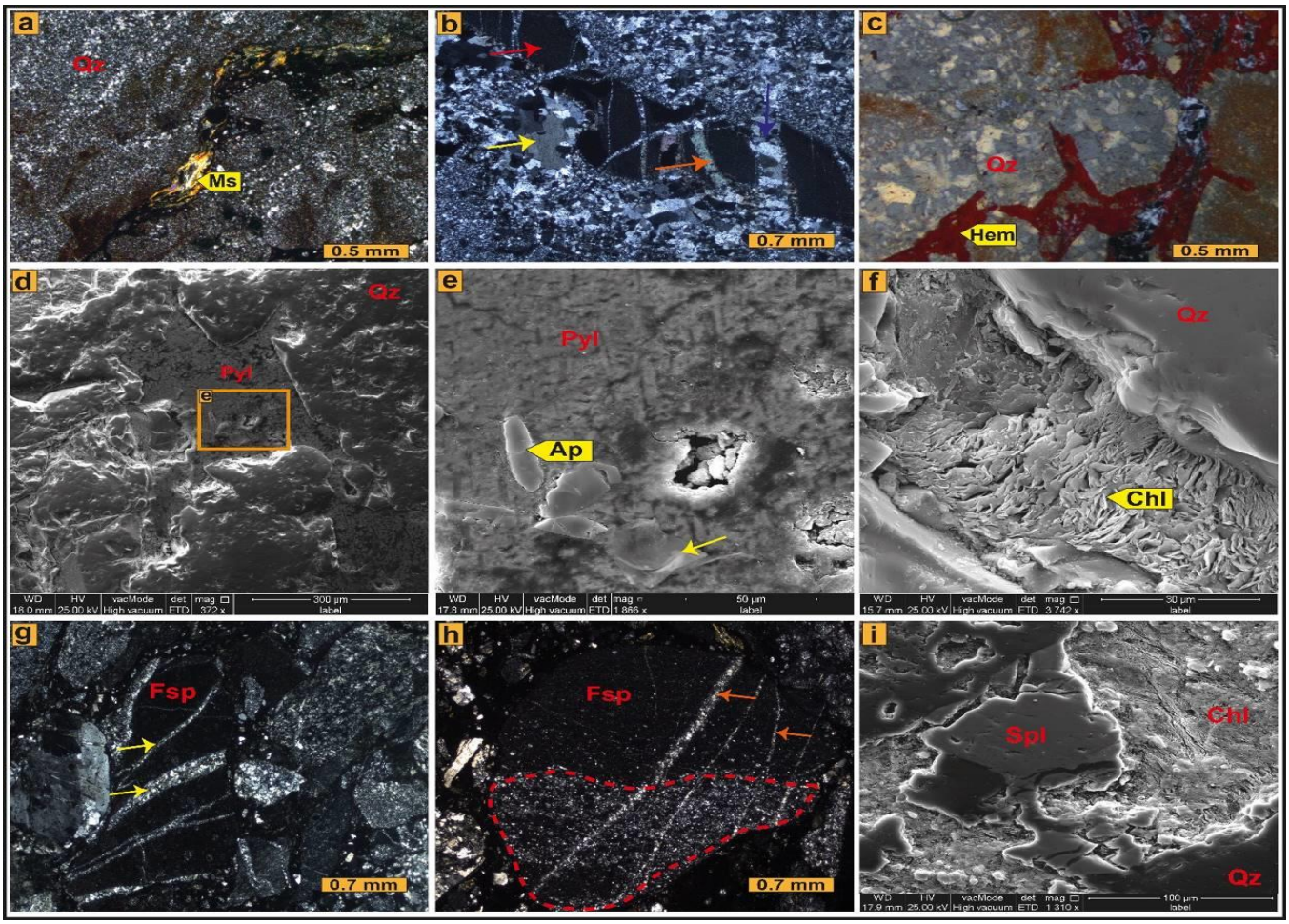

Figure 11: Photomicrographs of the SEM displaying the mineralogical constitution and microstructural properties of the chert (a-f) and transition zone (g-i). (a, b, c) quartz, and fine-grained silica as major components of chert. Quartz occurs as single crystals (yellow arrow in b), fine-grained material (reddish arrow), and veins (Blue arrow). Hematite is filling fractures and inter-spaces between minerals. In some instances, the quartz envelopes silica minerals. Calcite veins are also visible in the sample (orange arrow in b). Muscovite can be seen as elongated crystals filling the fractures (a); Pyrolusite is associated with quartz whereas apatite is associated with pyrolusite (d, e). It looks like an artifact; (f) Secondary chlorite flake-like crystals habit is filling fractures within silicate minerals; (g, h) show the mineral components of the transition zone in-between iron-rich bodies and calcareous sandstone. The transition zone comprises mainly quartz and feldspars. Feldspars are partially altered and, in most instances, replaced by quartz (reddish dashed line in h). It seems that before the replacement, the feldspars were enveloped and cross-cut by quartz veins (red and yellowish arrows in g, h); (i) spinel grains in the transition zone showing alteration on boundaries, pitting, and microporosity on the surface; (Ap: apatite, Chl: chlorite, Fsp: Feldspar, Hem: hematite, Ms: Muscovite, Pyl: pyrolusite, Qz: quartz, and Spl: spinel).

4.2.4. Calcareous Sandstone (CSd):

The main components of this rock are feldspar and quartz, along with altered fossils. The other component contains calcite and chlorite. Quartz is formed either as a very fine matrix or as veins that crosscut feldspars (Fig.12a, b, and c). Coralline red algae and nummulite represent highly altered fossils and the replaced by calcite (Fig.12b and c).

Tikrit Journal of Pure Science (2023) 28 (5): 74-106
Doi: https://doi.org/10.25130/tjps.v28i5.1584

4.2.5. Serpentinite (Serp):

The mineralogy of serpentinite is dominated by serpentine group minerals, including calcite, lizardite, and chrysotile, with pyroxene and magnetite, and a minor amount of spinel (Table 1). In the thin section, the serpentinite includes mesh-textured serpentines after pyroxene (Fig.12e). In most cases, spinel is converted to magnetite by alteration in the rims, and only some remnants of it remain (Fig.12f).

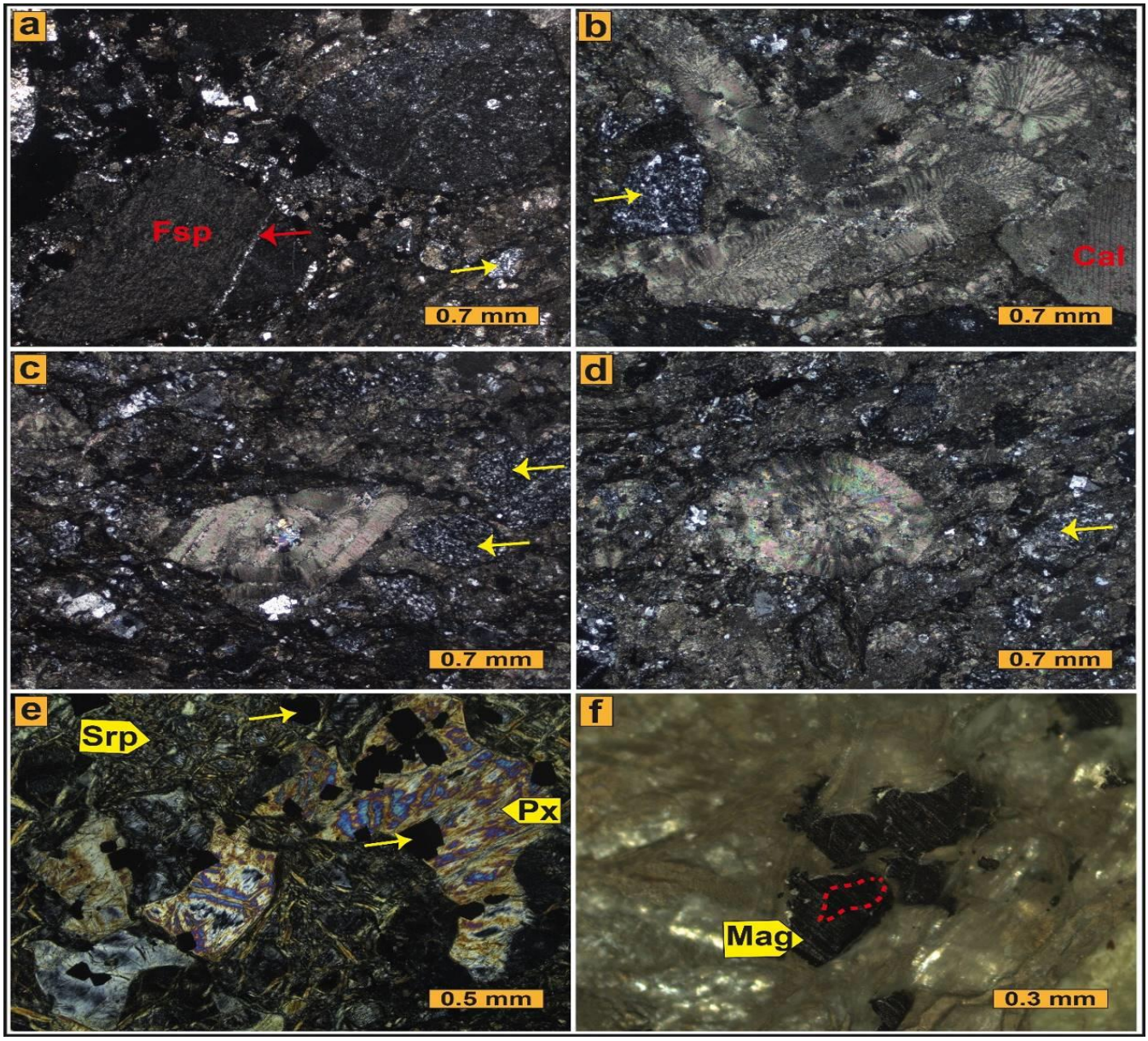

Figure 12: Optical photomicrographs displaying the mineralogical constitution and microstructural properties of the calcareous sandstone (a-d), and serpentinite (e f). (a-d) show quartz and feldspar as the main components of the rock. Quartz crystals are generally present as very fine matrix (yellow arrows) and vein (red arrow). The other component is calcite. Calcite is formed as a single crystal and, in most cases, it replaced fossils (b-d); (b-d) the highly altered fossils forms are coralline red algae and nummulite; (e and f) serpentine as mesh texture in serpentinite. There are some visible remains of primary minerals like pyroxene. Magnetite is formed by the serpentinization process of primary minerals, such as olivine and pyroxene. The other component is spinel. The spinel (reddish dashed line and orange arrow in f) is converting to magnetite and only some remnant of it has remained. (Fsp: feldspar, Mag: magnetite, Px: pyroxene, Qz: quartz, and Spl: spinel).

4.3. Fossil Bacteriomorphs:

A SEM analysis of thin sections, slabs, and chips from the iron-rich bodies indicates presence of microbial assemblages that are well-preserved, abundant, and matrix-embedded. Extracellular Polymeric Substances (EPSs) biofilms and microbial mat remnants are also present. The sedimentary nature of the rock formations during transportation and deposition are active environments for microbial involvement in neo-mineral formation or alteration of former minerals. The microbial interaction plays an active role in iron and calcite formations. Fossil microbial EPS layers at various level of preservation can be seen in the sample (Fig.13a, b, e, and f). These organic microbial matters, usually associated with bacteria and fungi, are sites for biomineralization as is shown in the mentioned figures. The calcite mineral crystals deposited on the EPS material are formed and induced by microbial interaction. Bacterial forms are visible in well-preserved and embedded fossils in rock matrix (Fig.13b, c, and d). The bacterial forms as the whole substrates in were subjected probably to the last phase of mineralization initiated by hydrothermal fluids causing silicate- Fe crystals deposition on the organic as well as minerals substrates (Fig.13b, c, and d).

Tikrit Journal of Pure Science (2023) 28 (5): 74-106
Doi: https://doi.org/10.25130/tjps.v28i5.1584

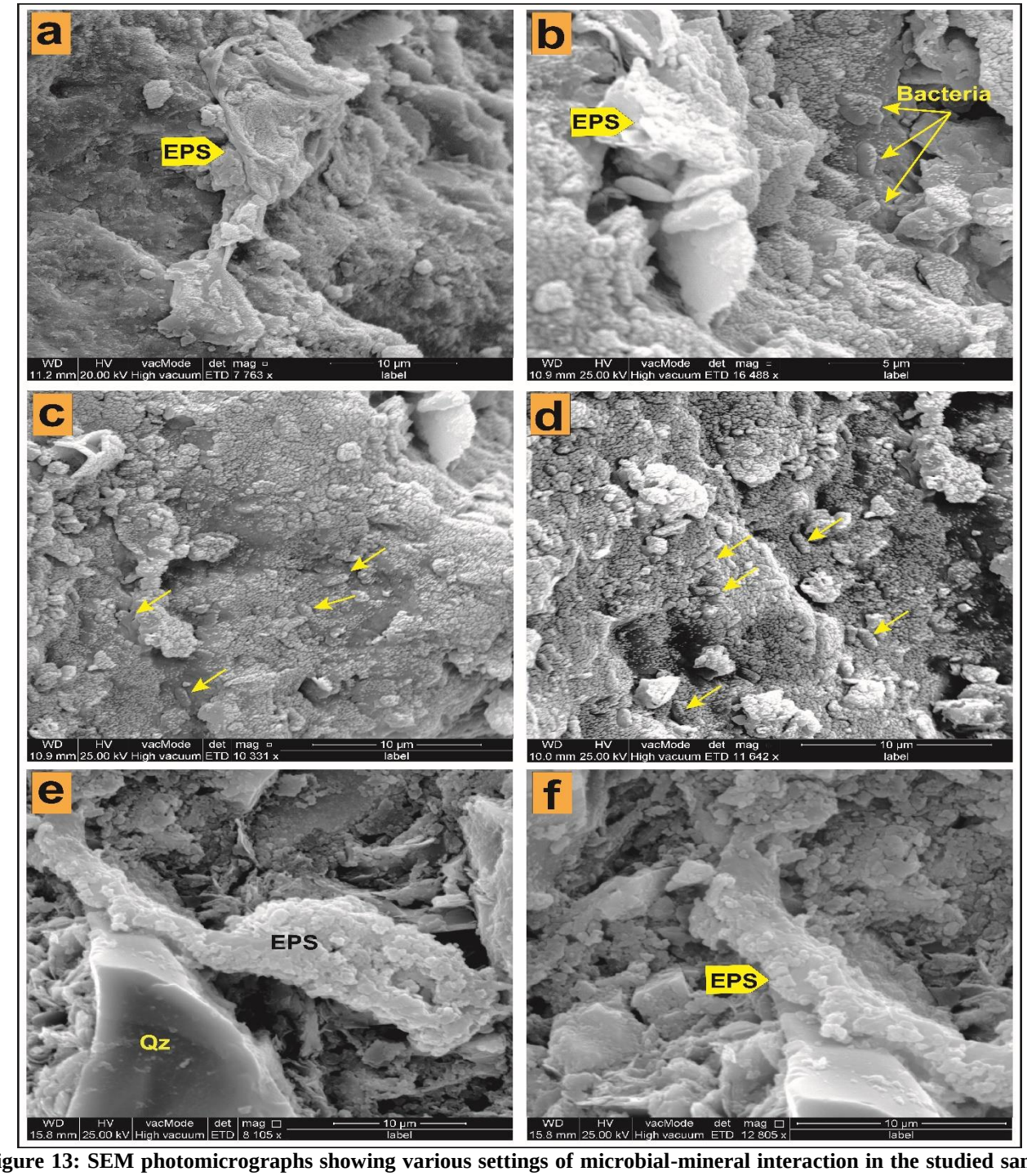

Figure 13: SEM photomicrographs showing various settings of microbial-mineral interaction in the studied samples. The sedimentary nature of the rock formations during transportation and deposition are active environments for microbial involvement in neo-mineral formation or alteration of former minerals. The microbial interaction plays an active role in iron and calcite formation. (a, b, e, and f) show fossil microbial EPS layers at various level of preservation. This organic microbial matter, usually associated with bacteria and fungi, are sites for biomineralization as is shown in the mentioned figures. The calcite mineral crystals deposited on the EPS material are formed and induced by microbial interaction. Fossils well-preserved and embedded in rock matrix bacterial forms are visible in (b, c, and d). The bacterial

(yellow arrow) forms as the whole substrates in (b, c, and d) were subjected probably to the last phase of mineralization initiated by hydrothermal fluids causing silicate- Fe crystals deposition on the organic as well as minerals substrates.

4.4. Mineral Chemistry:

The mineral chemistry of the iron-rich bodies and associated rocks of the area is shown in Table 2. SEM-EDS results show that the iron-rich bodies samples have a high content of Fe_2O_3 and SiO_2 in the ranges of 0.55–92.18 wt.% and 1.30–98.08 wt.% respectively. The concentration of Fe_2O_3 is high in hematite and magnetite, and chromite has a high concentration of Cr_2O_3, Fe_2O_3, and Al_2O_3. In sample A-3, apatite has been identified, which shows a high concentration of CaO (58.43 wt. % on average).

Quartz in cherts clasts shows on avg. 96.42 wt.% of SiO_2 and apatite with avg. 95.76 wt.% CaO. The concentration of MnO in pyrolusite and serandite are 68.008 and 37.12 wt.% on average, respectively. The chromite in the chert is rich in Cr_2O_3, Fe_2O_3, and Al_2O_3 (49.20 wt.%, 18.70 wt.%, and 17.32 wt.% on average, respectively); moreover, Cr_2O_3, Fe_2O_3, Al_2O_3, and SiO_2 show high concentration in spinel. Chlorite is rich in MgO, SiO_2, Al_2O_3, and Fe_2O_3 (20.46 wt.%, 31.18 wt.%, 19.39 wt.%, and 12.21 wt.% on average, respectively); also, Ni has a high concentration in chlorite at 8.88 wt.% on average (Fig.14).

In the transition zone, the concentration of SiO_2 in the quartz is 98.28 wt.% and that of Fe_2O_3 in the hematite is 88.486 wt.%. The ilmenite is rich in TiO_2 (avg. 95.84 wt.% TiO_2), whereas titano-magnetite is rich in TiO_2, SiO_2, Al_2O_3, MgO, and Fe_2O_3 (37.13 wt.% of TiO_2, 21.62 wt.% of SiO_2, 15.49 wt.% of Al_2O_3, 11.11 wt.% of MgO, and 10.42 wt.% of Fe_2O_3 on average, respectively). The identified feldspar containing SiO_2, Al_2O_3, Na_2O, and K_2O in the range of 60.35 wt.%, 23.65 wt.%, 7.99 wt.%, and 5.05 wt.% on average, respectively.

Sample A-31 from the serpentinite is composed of serpentine with avg. 47.90 wt.% of SiO_2 and avg. 42.43 wt.% of MgO, and hematite with avg. 88.34 wt.% of Fe_2O_3. Chromite is rich in Cr_2O_3 (avg. 41.48 wt.%) and Fe_2O_3 (avg. 34.80 wt.%); it also displays enrichment in MgO (avg. 8.12 wt.%), SiO_2 (avg. 6.90 wt.%), and Al_2O_3 (avg. 5.06 wt.%). Calcite is rich in CaO (avg. 85.42 wt.%).

Tikrit Journal of Pure Science (2023) 28 (5): 74-106
Doi: https://doi.org/10.25130/tjps.v28i5.1584

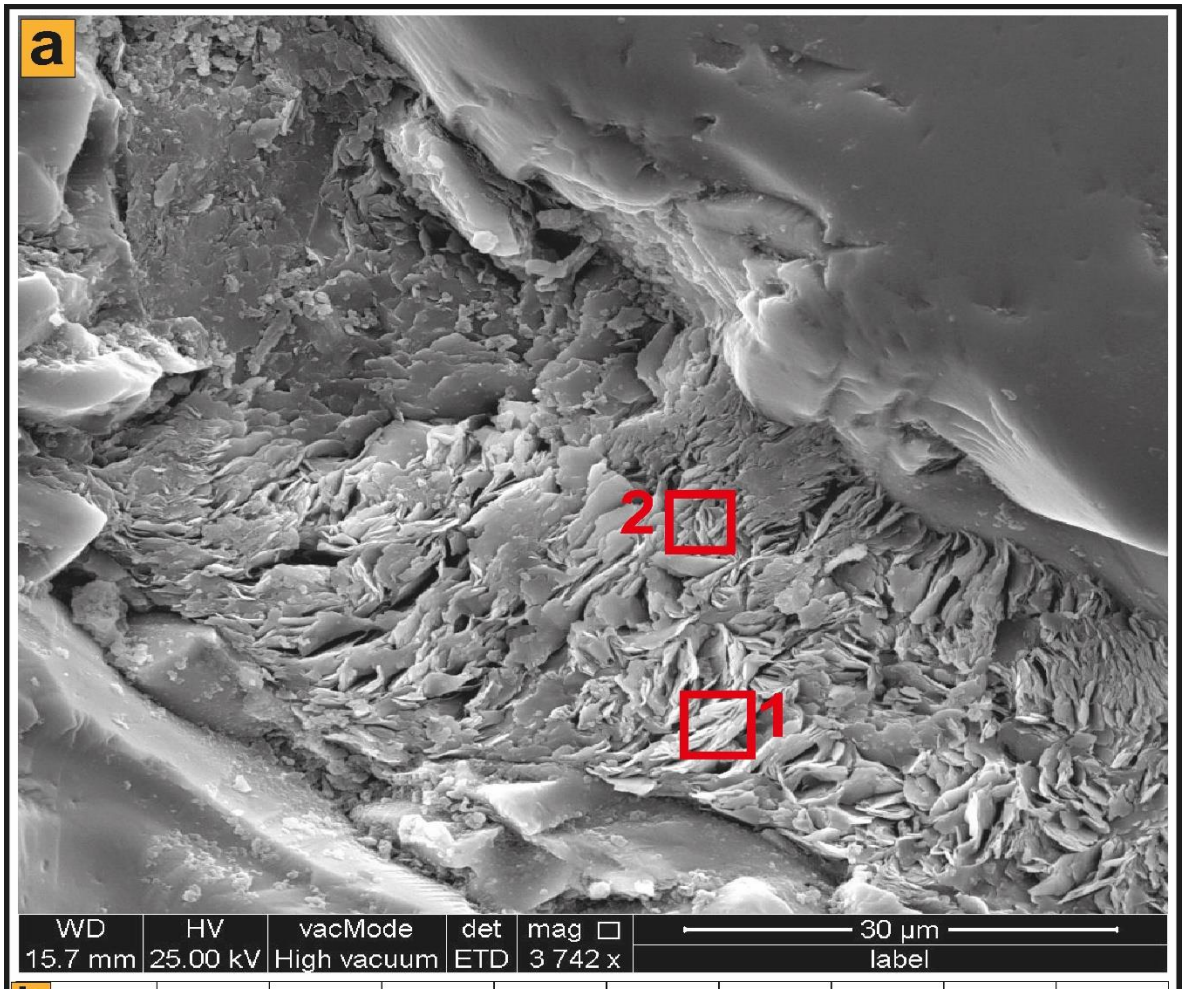

b

Point	SiO_2	Al_2O_3	MgO	Fe_2O_3	MnO	K_2O	Cr_2O_3	Co	Ni
1	31.84	19.16	19.91	12.37	1.01	0.01	4.12	0.46	9.22
2	30.52	19.62	21.02	12.05	1.12	0.08	4.48	0.79	8.54

Fig.14. (a) SEM image of chlorite in a chert sample; (b) SEM-EDS results of two points of chlorite.

Tikrit Journal of Pure Science (2023) 28 (5): 74-106
Doi: https://doi.org/10.25130/tjps.v28i5.1584

TJPS

Table 2: SEM-EDS results of mineral composition of Rayat iron-rich bodies and associated rocks (wt.% on average).

Type	S.No	Mineral	Na_2O	MgO	K_2O	CaO	TiO_2	Cr_2O_3	MnO	Fe_2O_3	Al_2O_3	SiO_2	S	Sc	V	Co	Ni	Cu	Zn	As	Ag	Ba	La	Ce	Pb
IRB	A-3	Quartz	0.00		0.01	0.06	0.06	0.14	0.09	0.55	0.66	98.08	0.15	0.02	0.00	0.06		0.00	0.02				0.00	0.02	
		Chromite	0.53	9.52	0.02	0.05	0.04	47.97	1.61	17.75	18.88	2.27	0.09	0.00	0.05	0.21	0.03	0.08	0.37	0.00	0.03		0.02	0.36	0.00
		Apatite	0.01	0.00	0.03	58.43				0.70	0.07	1.28	0.08	0.05		0.01	0.02	0.04	0.02	0.10			0.02	0.03	
		Hematite	1.97	2.70	0.11	0.16	0.05	0.40	0.12	83.53	3.58	5.03	0.10	0.00	0.05	0.87	0.7	0.16	0.10	0.03	0.00	0.05	0.06	0.05	0.07
		Spinel	0.44	5.54	0.37	0.68	0.18	11.94	0.73	8.89	55.06	13.14	0.19	0.00	0.03	0.24	1.83	0.12	0.11	0.08	0.00	0.00	0.15	0.17	
		Chlorite	0.82	4.60	0.17	0.44	0.06	0.18	0.12	57.52	16.44	15.50	0.04	0.05	0.02	0.58	2.10	0.18	0.07			0.07	0.10	0.09	0.71
IRB	A-20	Quartz			0.03	0.00		0.07	0.04	3.95	0.41	94.76	0.08	0.02		0.1	0.16	0.05	0.00			0.01	0.10	0.02	0.12
		Chromite		11.73		0.01	0.02	42.22	0.24	16.19	27.05	1.15	0.15		0.09	0.13	0.11	0.03	0.09	0.09	0.01		0.18	0.40	0.01
		Hematite	1.07	2.65	0.40	0.15	0.09	1.08	0.11	75.78	4.66	11.46	0.31	0.04	0.00	0.84	0.85	0.14	0.14	0.03	0.01	0.02	0.01	0.00	0.06
		Feldspar	0.53	4.38	9.50	0.1	0.03	1.14	0.06	19.73	21.04	42.19	0.07	0.00	0.01	0.16	0.67	0.03	0.00	0.02		0.04	0.00	0.00	0.19
		Magnetite	0.78	0.61	0.00	0.12	0.21	1.28	0.11	92.18	1.17	1.30	0.04	0.00	0.01	0.94	0.53	0.32	0.07	0.00	0.01	0.04	0.01	0.03	0.14
		Chlorite	0.52	15.65	0.19	0.48	0.18	0.67	0.34	33.94	21.48	21.05	0.09	0.06	0.00	0.69	4.30	0.07	0.07			0.08	0.03	0.00	
Chert	A-9	Quartz	0.00	0.05	0.04	0.03	0.02	0.03	0.09	1.46	0.64	96.42	0.83	0.01	0.01	0.02	0.07	0.03	0.01				0.04	0.06	
		Unknown Mineral	1.60	4.87	0.07	0.30	0.21	0.37	0.01	42.39	4.71	41.81	1.41		0.02		0.93		0.19		0.06		0.05	0.04	
		Chromite	1.02	10.30	0.00	0.10	0.20	49.2	0.29	18.70	17.32	1.48	0.20	0.00	0.08	0.18	0.16	0.16	0.16	0.04	0.02		0.11	0.13	0.06
		Spinel	2.07	7.70	0.17	2.34	0.10	33.76	2.52	15.58	19.94	13.63	0.75	0.02	0.03	0.12	0.61	0.10	0.29	0.03					0.16
		Pyrolusite	0.70	1.96	0.04	5.53	0.07	0.20	68.00	2.08	3.71	5.30	0.24	0.03	0.04	0.33	0.47	9.41	0.24			1.41	0.07	0.08	
		Apatite		0.00	0.00	95.76	0.12	0.38	1.80	0.26	0.12	0.45		0.21	0.02	0.04	0.02	0.40		0.04		0.11	0.07	0.13	
		Serandite	1.00	1.50	0.02	3.14		0.09	37.12	3.70	6.16	41.72	0.29			0.10	0.25	4.44	0.12	0.03	0.00	0.24			
		Chlorite	0.05	20.46	0.04	1.07	0.03	4.30	1.06	12.21	19.39	31.18	0.14	0.03	0.02	0.62	8.88	0.08	0.15		0.01	0.01	0.03	0.16	
TZ	A-12	Quartz	0.02	0.01	0.07	0.01	0.05	0.05	0.01	0.15	0.85	98.28	0.16	0.01	0.00	0.01	0.02	0.04	0.01		0.01	0.00	0.06	0.03	0.05
		Hematite	1.08	0.94	0.05	1.74	2.24	0.40	0.05	88.48	1.46	2.31	0.07	0.02	0.00	0.49	0.40	0.14		0.06					
		Chromite	0.68	10.96		0.01	0.17	49.36	0.03	18.39	18.27	1.21	0.16	0.00	0.09	0.13	0.13	0.05	0.00	0.01	0.00	0.08	0.07		0.10
		Feldspar	7.99	0.42	5.05	0.42	0.69	0.03	0.01	0.85	23.65	60.35	0.16	0.00	0.00	0.02	0.05	0.00	0.00	0.01		0.09	0.03	0.01	0.04
		Ilmenite			0.02	0.11	95.84			1.84		0.69					0.09	0.05			0.01		1.08		0.2
		Calcite	3.13	1.28	0.07	71.91	0.09	0.08	0.14	2.45	6.85	12.44		0.15	0.02	0.10	0.32	0.04				0.05	0.22	0.49	0.09
		Chlorite	1.64	17.07	1.15	0.95	0.39	1.40	0.37	15.40	22.05	36.37	0.15	0.01	0.00	0.17	2.59	0.00	0.00			0.03	0.02		0.16
		Titano-magnetite	1.84	11.11	0.03	0.44	37.13	0.13	0.25	10.42	15.49	21.62	0.19	0.00		0.10	0.99							0.02	0.15
		Unknown Mineral	1.21	11.02	0.23	0.95	1.59	0.84	0.20	54.79	9.04	17.61	0.10	0.01	0.01	0.20	1.55		0.03		0.01		0.01		0.50
Serp	A-31	Serpentine	0.11	42.43	0.01	1.22	0.03	0.41	0.05	4.44	2.59	47.9	0.19	0.00	0.02	0.05	0.30	0.02	0.00	0.00	0.00	0.02	0.02	0.03	0.07
		Calcite		6.69		85.42		0.04	0.07	0.87	0.61	5.58			0.04			0.23	0.04			0.04			0.31
		Hematite	2.48	2.18	0.01	0.14	0.11	0.11	0.28	88.34	1.91	2.12	0.16	0.01	0.00	1.22	0.28	0.32	0.04			0.04	0.10	0.01	0.04
		Chromite	0.16	8.12	0.00	0.32	0.57	41.48	0.56	34.8	5.06	6.90	0.17	0.01	0.13	0.32	0.08	0.04	0.08	0.01			0.26	0.72	0.09

4.5. Whole-Rock Geochemistry:

4.5.1. Major Elements:

Table 3 shows the chemical composition data of major elements (in weight percent). Generally, all the samples have a high content of SiO_2. The highest concentration of SiO_2 is in chert samples ranging between 74.97–80.52 wt.% which is more than the iron-rich bodies (27.08–66.41 wt.%), transition zone (42.74–77.05 wt.%), calcareous sandstone (50.63–66.38 wt.%), and serpentinites (33.13 and 39.84 wt.%).

The iron-rich bodies samples show Fe_2O_3 in ranges between 26.33–57.01 wt.%, whereas Fe_2O_3 of the chert is in the range of 9.08–18.49 wt.% and one of the transition zone's samples, which is closer to the IRBs, is 41.52 wt.%. Concentrations of Fe_2O_3 in serpentinites and calcareous sandstone is lower than 8 wt.%. The high amount of Cr_2O_3 recorded in iron-rich bodies samples is in the range of (1.58–3.12 wt.%).

The concentration of Al_2O_3 in iron-rich bodies, transition zone, calcareous sandstone, and chert is ranging from1.87–4.91 wt.%, 3.76–5.77 wt.%, 4.7–5.4 wt.%, and 1.68–3.21 wt.%, respectively, which have a higher range than the serpentinites with<1 wt. % concentration of Al_2O_3.

The serpentinites have a higher amount of MgO (30.15–34.38 wt.%) related to iron-rich bodies, the transition zone, calcareous sandstone, and chert, which have <5 wt.% MgO. CaO concentration in serpentinites and calcareous sandstone ranges between (1.79–9.92 wt.% and 9.72–18.72 wt.%, respectively). In almost all other horizons, the concentration of other major elements is <1 wt.%.

4.5.2. Trace and Rare Earth Elements:

Concerning the trace and rare earth elements listed in Table 3, the iron-rich bodies, transition zone, serpentinite, and chert have a higher concentration of Ni compared to Sr, whereas calcareous sandstone has a higher concentration of Sr compared to Ni. The concentration of Co and Zn in iron-rich bodies, transition zone, and chert is higher than in serpentinite and calcareous sandstone. The highest value of V is recorded in iron-rich bodies samples and one sample from the transition zone, while sulfur shows a higher amount in all samples except some samples of iron-rich bodies. The remaining elements have concentrations <100 ppm.

Total REE contents of the studied iron-rich bodies and associated rocks in most samples are very low. Generally, transition zone and calcareous sandstone samples show higher REE concentrations compared with iron-rich bodies, chert, and serpentinite samples. Chondrite-normalized REE patterns for iron-rich bodies (IRBs) and chert are displayed in (Fig.15). The chondrite-normalized REE spider diagrams of iron-rich bodies (IRBs) and chert are almost similar and show approximately flat REE patterns, with notable negative Ce, Tm, and Lu and positive Tb and Yb anomalies.

Tikrit Journal of Pure Science (2023) 28 (5): 74-106
Doi: https://doi.org/10.25130/tjps.v28i5.1584

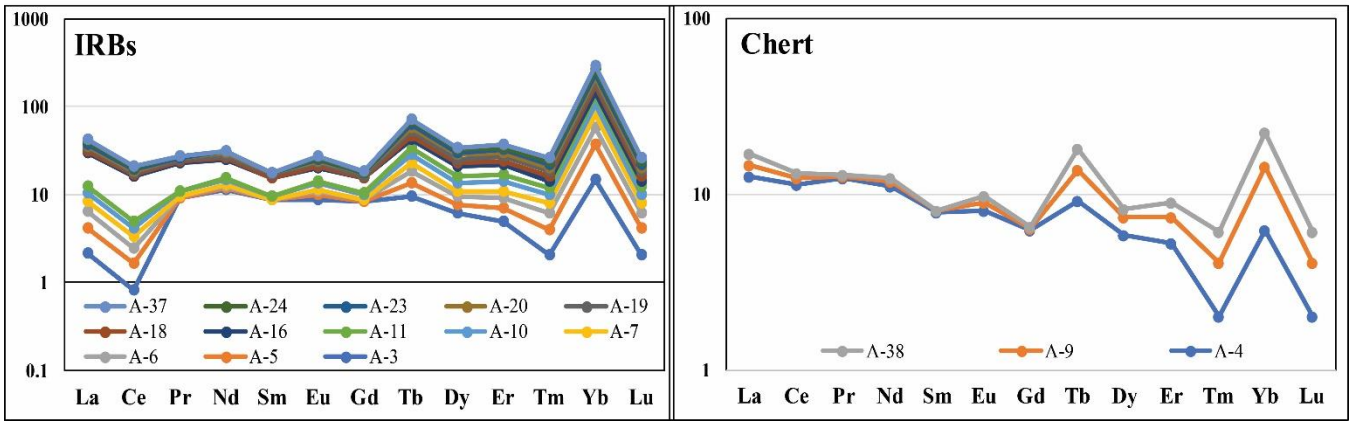

Figure 15: Chondrite normalized REE spider diagram patterns of the iron-rich bodies (IRBs) and Chert; normalization values are from [18].

Tikrit Journal of Pure Science (2023) 28 (5): 74-106
Doi: https://doi.org/10.25130/tjps.v28i5.1584

Table 3: ICP-OES and ICP-MS results of the Rayat iron-rich bodies and associated rocks.

Lith.[a]		IRBs													TZ		Serp		CSd		Chert		
Sample no.	**D.L.**	**A-3**	**A-5**	**A-6**	**A-7**	**A-10**	**A-11**	**A-16**	**A-18**	**A-19**	**A-20**	**A-23**	**A-24**	**A-37**	**A-12**	**A-13**	**A-31**	**A-40**	**A-34**	**A-36**	**A-4**	**A-9**	**A-38**
Major Oxides (wt.%)																							
SiO_2	0.05	66.41	31.87	41.1	29.66	28.66	41.58	55.69	30.05	36.75	28.19	30.27	27.08	27.14	77.05	42.74	33.13	39.84	66.38	50.63	80.52	75.93	74.97
Al_2O_3	0.05	1.87	4.33	3.75	4.21	4.43	4.19	4.83	4.22	4.11	4.77	4.06	4.91	4.55	5.77	3.76	0.6	0.47	5.4	4.7	3.21	1.68	1.87
CaO	0.05	0.47	0.28	0.19	0.26	0.44	0.3	0.14	0.54	0.53	0.63	0.81	0.47	0.34	1.04	0.5	9.92	1.79	9.72	18.72	0.65	0.91	0.18
Fe_2O_3	0.05	26.33	52.59	45.87	55.54	56.03	44.19	29.9	53.78	46.94	54.48	54.45	56.21	57.01	6.84	41.52	6.62	7.22	3.93	3.88	9.08	16.83	18.49
K_2O	0.05	0.26	0.68	0.69	0.72	0.87	0.98	1.66	0.47	0.69	0.63	0.6	0.98	0.64	0.8	0.08	0.025	0.025	0.96	0.5	0.08	0.35	0.29
MgO	0.05	1.2	2.98	2.28	2.6	2.61	2.62	2.33	3.45	2.95	3.47	2.83	3.01	3.18	2.68	4.49	30.15	34.38	3.12	2.79	2.7	1.07	1.39
MnO	0.05	0.19	0.25	0.22	0.22	0.29	0.22	0.14	0.15	0.15	0.17	0.22	0.18	0.2	0.09	0.15	0.06	0.12	0.05	0.07	0.15	0.25	0.08
Na_2O	0.05	0.13	0.025	0.025	0.025	0.025	0.06	0.11	0.05	0.06	0.07	0.025	0.025	0.025	1.62	0.17	0.09	0.025	0.41	0.61	0.4	0.025	0.025
P_2O_5	0.05	0.21	0.025	0.025	0.025	0.14	0.025	0.025	0.05	0.08	0.025	0.12	0.06	0.08	0.07	0.025	0.025	0.025	0.07	0.11	0.22	0.21	0.025
TiO_2	0.05	0.08	0.1	0.07	0.1	0.11	0.09	0.36	0.09	0.11	0.12	0.1	0.1	0.1	0.65	0.13	0.025	0.025	0.42	0.45	0.35	0.025	0.025
Cr_2O_3	0.05	1.58	2.82	2.6	3.01	2.79	2.51	1.77	2.93	2.6	2.93	2.59	3.12	2.97	0.025	2.25	0.025	0.025	0.025	0.025	0.025	0.9	1.01
LOI	0.05	1.05	2.98	2.42	2.77	2.7	2.53	2.48	3.24	4.18	3.39	3.13	3.09	2.82	2.65	3.64	18.86	15.54	9.47	17.37	1.94	1.51	1.31
Total		99.78	98.93	99.24	99.14	99.095	99.295	99.435	99.02	99.15	98.875	99.205	99.235	99.055	99.285	99.455	99.53	99.485	99.955	99.855	99.325	99.69	99.665
Trace Elements (ppm)																							
As	0.1	5.8	18.1	17.1	18.8	18.2	10.4	4.5	13.1	9.9	15.9	13	11.9	12.6	0.5	9.4	2.6	2.7	1.3	11.5	3.1	5.5	5.2
Ba	1	30	52	54	47	88	86	163	51	48	67	82	73	77	68	46	0.5	0.5	46	110	46	72	31
Co	1	189.1	678.5	512.8	654.5	610.1	626.1	293	589.3	572.4	624.7	486.4	478	582.1	194.6	305	85.9	94.6	12.9	11.8	226.1	258.9	291.7
Cs	1	1.3	2.7	2.5	3.2	4.1	2	4.3	1.9	2.4	3.1	2.6	2.7	2.7	1.5	0.6	0.25	0.9	1.4	0.8	0.25	1.2	0.9
Cu	1	53	7	6	6	4	10	12	4	4	59	5	4	2	24	29	2	18	20	16	22	28	10
Li	1	10	7	4	6	7	5	6	6	6	9	5	7	7	11	8	0.5	0.5	19	21	6	8	0.5
Mo	0.1	35	7	15	10	6	10	14	7	14	7	8	6	6	38	12	0.05	1	6	8	34	49	28
Nb	1	0.5	1.2	0.5	1.2	1.4	2.2	3.3	1.1	1.1	1.6	1.1	1.1	1.1	6.4	1.9	0.5	0.5	2.9	4	2.9	0.5	0.5
Ni	1	2094	9803	7536	8436	8180	6793	5175	8615	7691	9893	6970	6886	8413	2815	5132	1803	1888	101	90	3469	3750	4250
P	10	805	144	282	215	653	173	113	269	389	223	490	383	364	354	148	77	42	301	367	859	839	215
Pb	1	0.5	5	5	9	5	3	2	8	8	9	6	15	9	0.5	8	0.5	0.5	0.5	0.5	0.5	0.5	4
Rb	1	7	20	22	23	27	26	46	15	22	22	19	29	19	20	4	2	2	25	16	3	12	10
S	50	113	99	105	117	112	116	106	118	107	136	98	81	95	112	114	198	246	190	274	108	137	114
Sb	0.5	0.5	1.5	0.8	1.1	1.2	1.2	1	1.6	1.6	1.8	1.7	2	1.8	0.25	1.6	5.4	0.25	1.7	3.5	0.25	0.25	0.7
Sc	0.5	16	41.2	34.7	42.7	45	35	23.5	42.2	34.4	44	41.8	42	42.1	10.6	28.1	5	5.2	5.6	6.2	9.3	12.8	13.8
Sn	0.1	0.8	0.7	0.6	0.6	0.6	0.7	0.8	0.7	0.7	0.6	0.7	0.6	0.6	0.9	0.6	0.4	0.4	0.8	0.8	1.4	0.6	0.6
Sr	1	56.4	32.1	33.7	38.6	50.1	29.7	44.8	36.1	36.5	41.1	46	39.6	41.3	64.4	34.7	19.7	34.6	111.4	317.5	51.5	35.2	16.8
Ta	0.1	0.34	0.35	0.38	0.38	0.38	0.43	0.58	0.37	0.4	0.36	0.34	0.33	0.34	0.86	0.45	0.22	0.22	0.53	0.6	0.53	0.35	0.25
Th	0.1	0.05	0.05	0.05	0.05	0.05	0.05	0.35	0.05	0.05	0.05	0.05	0.05	0.05	0.69	0.05	0.05	0.05	0.68	0.62	0.05	0.05	0.05
U	0.1	0.3	0.3	0.2	0.3	0.3	0.3	0.4	0.3	0.4	0.4	0.3	0.3	0.3	0.3	0.8	0.05	0.05	0.6	1.2	0.2	0.2	0.1
V	1	202	203	187	222	205	197	151	197	188	208	180	208	196	59	255	26	21	63	77	89	79	89
Y	0.5	8.8	1.4	1.7	2	3.6	2.6	5.3	2.3	3.3	3.3	2.3	1.8	2.4	7.8	9.9	0.25	0.25	8.4	9.7	8.2	2.1	0.8
Zn	1	192	323	293	349	348	286	196	326	294	370	287	319	334	90	239	40	43	36	38	63	121	133
Zr	5	12	22	19	22	26	33	32	22	21	26	22	22	23	54	21	2.5	2.5	30	40	27	9	10

Tikrit Journal of Pure Science (2023) 28 (5): 74-106
Doi: https://doi.org/10.25130/tjps.v28i5.1584

Lith.[a]		IRBs													TZ		Serp		CSd		Chert		
Sample no.	**D.L.**	**A-3**	**A-5**	**A-6**	**A-7**	**A-10**	**A-11**	**A-16**	**A-18**	**A-19**	**A-20**	**A-23**	**A-24**	**A-37**	**A-12**	**A-13**	**A-31**	**A-40**	**A-34**	**A-36**	**A-4**	**A-9**	**A-38**
Rare Earth Elements (ppm)																							
La	1	0.5	0.5	0.5	0.5	0.5	0.5	4	0.5	0.5	0.5	0.5	0.5	0.5	4	5	0.5	0.5	8	10	3	0.5	0.5
Ce	1	0.5	0.5	0.5	0.5	0.5	0.5	7	0.5	0.5	0.5	0.5	0.5	0.5	11	2	0.5	0.5	15	18	7	0.5	0.5
Pr	0.05	0.83	0.025	0.025	0.025	0.1	0.025	1.14	0.025	0.16	0.09	0.025	0.025	0.025	1.37	1.04	0.025	0.025	1.66	2.01	1.14	0.025	0.025
Nd	0.5	5.1	0.25	0.25	0.25	0.9	0.25	4.5	0.25	1	1	0.25	0.25	0.25	6.2	4.7	0.25	0.25	6.4	8.2	5.1	0.25	0.25
Sm	0.02	1.29	0.01	0.01	0.01	0.11	0.01	0.86	0.01	0.2	0.06	0.01	0.01	0.01	1.35	1.09	0.01	0.01	1.24	1.56	1.17	0.01	0.01
Eu	0.1	0.5	0.05	0.05	0.05	0.1	0.05	0.35	0.05	0.11	0.05	0.05	0.05	0.05	0.48	0.54	0.05	0.05	0.41	0.56	0.45	0.05	0.05
Gd	0.05	1.67	0.025	0.025	0.025	0.28	0.09	0.91	0.025	0.23	0.24	0.025	0.025	0.05	1.24	1.53	0.025	0.025	1.35	1.59	1.25	0.025	0.025
Tb	0.1	0.35	0.15	0.17	0.17	0.19	0.19	0.3	0.17	0.2	0.21	0.18	0.15	0.17	0.35	0.38	0.12	0.13	0.36	0.38	0.33	0.17	0.15
Dy	0.02	1.54	0.34	0.42	0.42	0.68	0.58	1.22	0.46	0.63	0.65	0.52	0.45	0.46	1.43	1.95	0.14	0.11	1.61	1.74	1.44	0.37	0.23
Er	0.05	0.78	0.32	0.34	0.33	0.49	0.45	0.81	0.36	0.46	0.45	0.37	0.35	0.38	0.83	0.98	0.13	0.14	0.93	1.02	0.84	0.34	0.25
Tm	0.1	0.05	0.05	0.05	0.05	0.05	0.05	0.05	0.05	0.05	0.05	0.05	0.05	0.05	0.05	0.11	0.05	0.05	0.12	0.12	0.05	0.05	0.05
Yb	0.05	2.4	3.6	3.4	4	4.1	3.4	2.6	3.8	3.4	3.9	3.8	3.9	4	0.9	3.6	0.3	0.3	0.7	0.9	1	1.3	1.3
Lu	0.1	0.05	0.05	0.05	0.05	0.05	0.05	0.05	0.05	0.05	0.05	0.05	0.05	0.05	0.12	0.11	0.05	0.05	0.12	0.15	0.05	0.05	0.05

[a] Lithology: IRBs: iron-rich bodies, TZ: transition zone, Serp: serpentinites, CSd: calcareous sandstone

4.5.3. Concentration Factor:

The Concentration Factor (CF) for different lithologies of the studied area related to Upper Continental Crust (UCC) has been calculated (after[19]). Accordingly, CF for different lithologies revealed as following (Table 4): Serpentine is significantly enriched in MgO (x13), Co (x5.2), Ni (x39.27), and Sb (x7.5); IRBs are enriched in Fe_2O_3 (x9.67), Cr_2O_3 (x202.31), Co (x30.67), Mo (x10.4), and Ni (x157.91); and the cherts are enriched in Cr_2O_3, Co, Mo, and Ni with concentration factors of 50, 14, 33.64, and 81.34, respectively. The TZ shows enrichment in Fe_2O_3, Co, Mo, and Ni relative to UCC. The concentrations of Cr_2O_3, Mo, and Sb are elevated in CSd in comparison to UCC.

Table 4: Average geochemical composition of the IRBs and associated rocks and enrichment factors in comparison to Clark values (UCC values according to [19]).

Lith[a]	Serp	IRBs	Chert	TZ	CSd	Serp	IRBs	Chert	TZ	CSd	UCC
	Average Content					Concentration Factor					
Major Oxides (wt.%)											
SiO_2	36.45	36.45	77.14	59.9	58.51	0.55	0.55	1.16	0.90	0.88	66.62
Al_2O_3	0.54	4.18	2.26	4.765	5.05	0.04	0.27	0.15	0.31	0.33	15.4
CaO	5.86	0.42	0.58	0.77	14.22	1.63	0.12	0.16	0.21	3.96	3.59
Fe_2O_3	6.92	48.72	14.8	24.18	3.91	1.37	9.67	2.94	4.80	0.78	5.04
K_2O	0.025	0.76	0.24	0.44	0.73	0.01	0.27	0.09	0.16	0.26	2.8
MgO	32.27	2.73	1.72	3.585	2.96	13.01	1.10	0.69	1.45	1.19	2.48
MnO	0.09	0.2	0.16	0.12	0.06	0.90	2.00	1.60	1.20	0.60	0.1
Na_2O	0.058	0.05	0.15	0.895	0.51	0.02	0.02	0.05	0.27	0.16	3.27
P_2O_5	0.025	0.07	0.16	0.048	0.09	0.17	0.47	1.07	0.32	0.60	0.15
TiO_2	0.025	0.12	0.13	0.39	0.44	0.04	0.19	0.20	0.61	0.69	0.64
Cr_2O_3	0.025	2.63	0.65	1.138	0.025	1.92	202.31	50.00	0.01	87.54	0.013
Trace Elements (ppm)											
As	2.65	13.02	4.6	4.95	6.4	0.55	2.71	0.96	1.03	1.33	4.8
Ba	0.5	70.62	49.67	57	78	0.00	0.11	0.08	0.09	0.13	624
Co	90.25	530.54	258.9	249.8	12.35	5.22	30.67	14.97	14.44	0.71	17.3
Cs	0.58	2.73	0.74	1.05	1.1	0.12	0.56	0.15	0.21	0.22	4.9
Cu	10	13.54	20	26.5	18	0.36	0.48	0.71	0.95	0.64	28
Li	0.5	6.54	4.83	9.5	20	0.02	0.31	0.23	0.45	0.95	21
Mo	0.52	11.15	37	25	7	0.47	10.14	33.64	22.73	6.36	1.1
Nb	0.5	1.33	1.3	4.15	3.45	0.04	0.11	0.11	0.35	0.29	12
Ni	1845.5	7421.92	3823	3973.5	95.5	39.27	157.91	81.34	84.54	2.03	47
P	59.5	346.39	637.67	251	334	0.09	0.53	0.97	0.38	0.51	655
Pb	0.5	6.5	1.67	4.25	0.5	0.03	0.43	0.11	0.28	0.03	15
Rb	2	22.85	8.33	12	20.5	0.02	0.27	0.10	0.14	0.24	84
S	222	107.93	119.67	113	232	0.36	0.17	0.19	0.18	0.37	621
Sb	2.82	1.37	0.4	0.93	2.6	7.05	3.43	1.00	2.33	6.50	0.4
Sc	5.1	37.28	11.97	19.35	5.9	0.36	2.66	0.86	1.38	0.42	14
Sn	0.4	0.67	0.87	0.75	0.8	0.19	0.32	0.41	0.36	0.38	2.1
Sr	27.15	40.46	34.5	49.55	214.45	0.08	0.13	0.11	0.15	0.67	320
Ta	0.22	0.38	0.38	0.66	0.57	0.24	0.42	0.42	0.73	0.63	0.9
Th	0.05	0.073	0.05	0.37	0.65	0.00	0.01	0.00	0.04	0.06	10.5
U	0.05	0.32	0.17	0.55	0.9	0.02	0.12	0.06	0.20	0.33	2.7
V	23.5	195.7	85.67	157	70	0.24	2.02	0.88	1.62	0.72	97
Y	0.25	3.14	3.7	8.85	9.05	0.01	0.15	0.18	0.42	0.43	21
Zn	41.5	301.3	105.67	164.5	37	0.62	4.50	1.58	2.46	0.55	67
Zr	2.5	23.23	15.33	37.5	35	0.01	0.12	0.08	0.19	0.18	193

Table 4: Continued

Lith.[a]	Serp	IRBs	Chert	TZ	CSd	Serp	IRBs	Chert	TZ	CSd	UCC
	Average Content					Concentration Factor					
Rare Earth Elements (ppm)											
La	0.5	0.77	1.33	4.5	9	0.02	0.02	0.04	0.15	0.29	31
Ce	0.5	1	2.66	6.5	16.5	0.01	0.02	0.04	0.10	0.26	63
Pr	0.025	0.2	0.4	1.205	1.835	0.00	0.03	0.06	0.17	0.26	7.1
Nd	0.25	1.12	1.87	5.45	7.3	0.01	0.04	0.07	0.20	0.27	27
Sm	0.01	0.2	0.39	1.22	1.4	0.00	0.04	0.08	0.26	0.30	4.7
Eu	0.05	0.12	0.18	0.51	0.485	0.05	0.12	0.18	0.51	0.49	1
Gd	0.025	0.28	0.43	1.385	1.47	0.01	0.07	0.11	0.35	0.37	4
Tb	0.125	0.2	0.21	0.365	0.37	0.18	0.29	0.30	0.52	0.53	0.7
Dy	0.125	0.64	0.68	1.69	1.675	0.03	0.16	0.17	0.43	0.43	3.9
Er	0.135	0.46	0.47	0.905	0.975	0.06	0.20	0.20	0.39	0.42	2.3
Tm	0.05	0.05	0.05	0.08	0.12	0.17	0.17	0.17	0.27	0.40	0.3
Yb	0.3	3.57	1.2	2.25	0.8	0.15	1.79	0.60	1.13	0.40	2
Lu	0.05	0.05	0.05	0.115	0.135	0.16	0.16	0.16	0.37	0.44	0.31

[a] Lithology: IRBs: iron-rich bodies, TZ: transition zone, Serp: serpentinites, CSd: calcareous sandstone

5. Discussion:

The geochemical data shows high contents of Fe_2O_3 and SiO_2 in the iron-rich bodies and high contents of SiO_2 in the associated rocks. The presence of pyrolusite in chert indicates a high MnO concentration. High CaO concentrations indicate the existence of common carbonates like calcite. The high concentration of Cr-spinel indicates enrichment according to Cr, Co, and V. Ni association with iron oxide results from the existence of hematite's strong metal-binding [20]; however, the SEM-EDS data show that in chlorite, Ni has a high concentration (Fig. 14). According to concentration factor the studied lithologies generally show high potential for mineralization of Fe, Cr, Ni and Co and as well as for Mo and Sb. In Rayat area, the relationships between the strata of the field and the studied profiles' geochemical and mineralogical characteristics suggest a sulfide hydrothermal deposition combination at the seafloor and sub-seafloor interface, succeeded by Fe mineralization of the Algoma-type, attended by subsequent oxidation and activities of hydrothermal exhalative. Due to the dominance of the Fe-rich lithofacies, chemical sedimentation processes ensured that the whole process occurred in a marine depositional environment [21; 22]. However, the lithologies are more enriched in Fe, Co, Ni, and Cr than in Cu. Therefore, at least in the sections examined here, it appears that the Choman-Rayat iron-rich bodies are not directly connected to the volcanogenic massive sulfide (VMS). The higher concentration of P_2O_5 might be owing its existence to apatite, while P bonding to hematite cannot be eliminated [23]. Moreover, the formation of apatite in sedimentary basins can be well interpreted as a result of microbial mediation, where dissolved phosphorous by microbes can be precipitated as a sedimentary mineral [24]. The samples containing manganese oxides; Mn is a component of the pyrolusite minerals. Ce as an REEs, is depleted in some samples, which is due to the increased mobility of these elements as a result of weathering or alteration (Fig. 15) [25]. However, the small positive Eu, the negative Ce anomaly, and the low Nd

concentrations together with the low REE concentrations in the IRBs and chert refer to a hydrothermal origin for these rock types [26; 27].

The geochemical data diagrams [28; 29; 30] show that the analyzed iron ore mineralization is of sedimentary type (Figs. 16 and 17). Data plots on the Ba-Fe_2O_3 diagram fall in the sedimentary BIF (Fig.16). Data on trace elements in iron-rich bodies and chert samples are plotted on the volcano-sedimentary and hydrothermal iron ores field in V/Ti vs. Ni/Ti diagram (Fig.17a). The iron-rich bodies data on V vs. Ni diagrams (Fig.17b) are plotted on the borderline between sedimentary and apatite iron ores due to the high concentration of Vanadium. Nevertheless, this high concentration of V can be attributed to the association with clay and organic matter [31]. Bacterial involvement in V precipitation cannot be excluded, especially by meso- and thermophilic methanogenic bacteria [32] or through the adsorption of Vanadyl ion (VO^{2+}) to settling sediment particle surfaces in the marine sedimentary environment [33]. The high vanadium concentrations of rocks deposited in marine environments as compared to lacustrine environments are the outcome of the relatively large amount of vanadium provided by circulating ocean water compared to terrestrial runoff [32; 34; 35]. Similarly, the data on the Co vs. Ni and V vs. Ni + Co diagrams are plotted on the volcano-sedimentary and hydrothermal iron ores field (Fig.17c and d). These types of iron-rich bodies are regarded as having a sedimentary origin from a genetic perspective [36].

In the sedimentary context only, enrichment of Fe and SiO_2 and microbial involvement under hydrothermal conditions are comparable to the modern BIF analogue of millimeter-thick alternating sedimentary Fe-rich and SiO_2-rich layers reported by Chi Fru [37], where oxidation-reduction conditions alternated under a hydrothermal system. Both biological and non-biological models of formation were inferred [37]. Moreover, Pirouei [9] reported the occurrence of BIF-like Fe-SiO_2 alternating layers in Rayat area. Microbial involvement in Fe enrichment and the formation of BIFs is well known and is a bio-physio-chemical process within ancient sedimentary environments [38].

In relation to other group of metals, the Walash-Naopurdan Group comprises chromite mineralization and is also altered by hydrothermal activities [39]. Cr-spinel is a common mineral in iron-rich bodies and associated rock in Rayat area. Because the serpentinites and serpentinized peridotites in the broader area also contain a high amount of Cr-spinel [40], it is possible that the peridotites and serpentinites are the sources of Cr-spinel, supplying more evidence that serpentinites are the parent rock of the observed mineralization. Magnetite is formed secondarily in serpentinites, mostly as an alteration product of Cr-spinels. In some cases, the rims of Cr-spinels are altered to magnetite (Fig.12f).

The bio-sedimentary (Figs.9, 11, and 12) attributes of the studied samples show fossil red algae and foraminiferas partially or totally mineralized due to the dissolution-precipitation process and fossil microbial content comprising mineralized bacteria and EPS material. The diagenetically altered fossils, mineral-coated bacteria, and EPS material suggest hydrothermal effects

that probably occurred at different stages, the last of which was bacterial mineralization. In one instance, within the fossil mineralization context (Fig.10e), observed alternating sub-millimeter-thick layers of Fe-rich layers suggest hydrothermal conditions [38].

Field sedimentological features of iron-rich bodies, petrographic data, such the grain morphology, the presence of serpentinites and detrital Cr-spinel generated from the surrounding ultramafic rocks, and the co-occurrence of different fossil types, all show that the iron-rich bodies had formed in significant part during the sedimentary processes. The exact timing of the iron-rich bodies' formation is unidentified, however, the area's general geological history suggests that they formed during the Paleocene-Eocene period [41; 42].

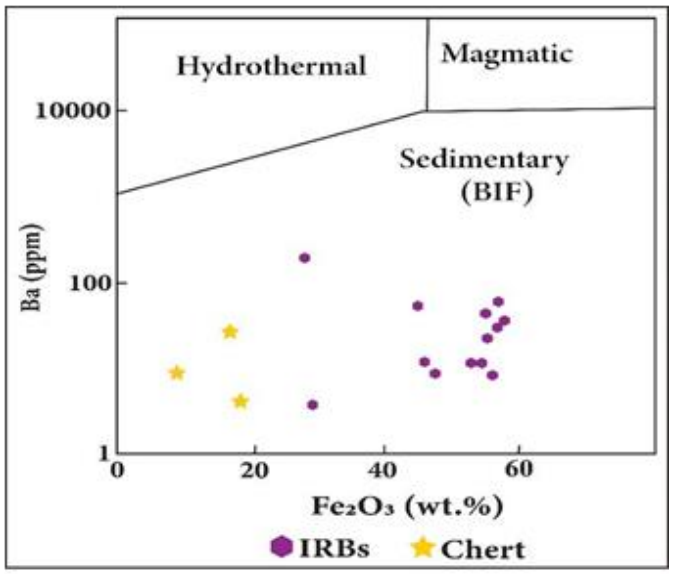

Figure 16: The plots of iron-rich bodies and chert samples from Rayat area on Ba-Fe_2O_3 geochemical diagrams (after[28]).

Tikrit Journal of Pure Science (2023) 28 (5): 74-106
Doi: https://doi.org/10.25130/tjps.v28i5.1584

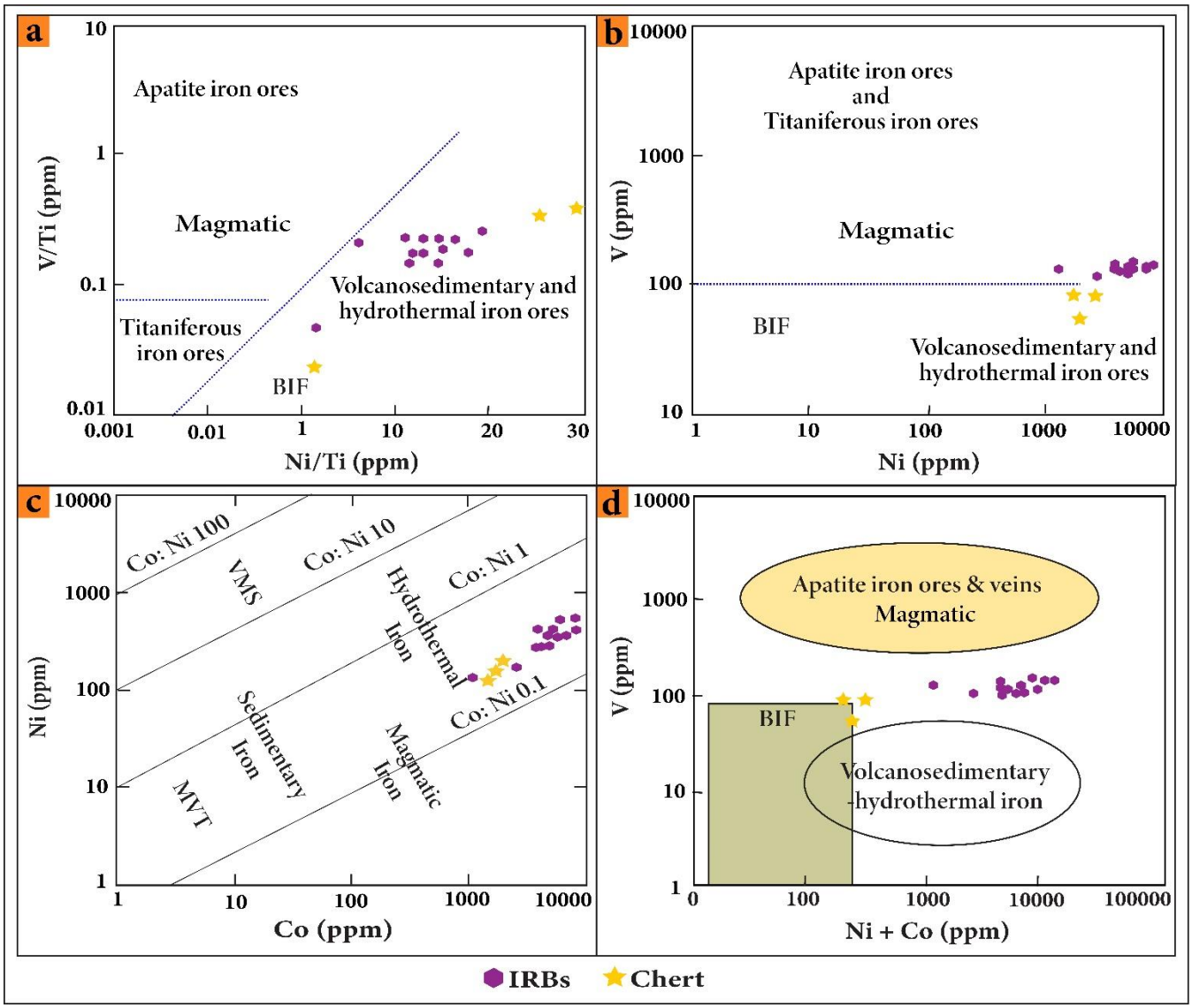

Figure 17: The plots of iron-rich bodies and chert samples from Rayat area on geochemical diagrams; (a) V/Ti vs. Ni/Ti and (b) V vs. Ni diagrams are (after [29]); (c) Co-Ni diagram (after [30]); (d) V vs. Ni+Co diagram (after [29]).

6. Conclusions:

The Rayat mountainous area exhibited an interesting assemblage of lithologies. The outcrops are characterized by ultramafic rock types, main serpentinites with high chromite content, and breccia with polymictic chlorite cementation with ultramafic clasts. Though the area contains brecciated layers that are rich in minerals containing iron, quartz and/or chalcedony are the most common minerals in iron-rich bodies and chert hematite, while Cr-spinels are also present. In all samples, hematite is the primary matrix. In Fe-rich mineralized zones, the elements Fe, Ni, Cr, and Mn are significantly enriched. According to concentration factor the studied lithologies generally show high potential for mineralization of Fe, Cr, Ni and Co and as well as for Mo and Sb. The overall characteristics of the lithological alternation, together with geochemical and mineralogical data, lead to sedimentary and hydrothermal iron mineralization occurring in a marine environment. The Walash Group's brecciated serpentinite, which is a constituent of the ophiolitic mélange, is the altered wall rock's parent rock.

The discovery of these iron-rich bodies in Choman-Rayat area provides a significant contribution to Kurdistan's geology and the potential for identifying new economic mineralization-rich areas, and for the ornamental industry, it can be a good potential raw mineral; moreover, to fully assess any economic potential, more thorough resource definition studies are needed.

5. References:

1. Bolton, C., *Geological map, kurdistan series, scale 1/100000, sheet k6 halabja*. 1954.
2. Bolton, C., *Report on the geology and economic prospect of the qala dizeh area site inv.* Co. Report, SOM, 1955.
3. Vasiliev, M. and V. Pentelkov, *Prospecting-exploration of the bard-i-zard chromite occurrence & adjacent areas in 1961*. 1962.
4. Jassim, S.Z. and J.C. Guff, *Geology of iraq.* Dolin Prague and Moravian Museum: Brno, Czech., 2006.
5. Fouad, S., *Tectonic map of iraq, scale 1: 1000 000, 3rd edit.* GEOSURV, Baghdad, Iraq, 2012.
6. Al-Bassam, K., *Mineral resources of kurdistan region, iraq.* Iraqi Bulletin of Geology and Mining, 2013. **9**(3): p. 103-127.
7. Shingaly, W.S., A.I. Al-Juboury, and E.M. Elias, *The role of carbonate-host rocks on the genesis of pb-zn deposits, northern thrust zone, kurdistan region, iraq.* Journal of Tethys: Vol, 2015. **3**(1): p. 031-047.
8. MNR, *Occurrences of metallic deposits in the kurdistan region, iraq. Kurdistan regional government.* 2016.
9. Pirouei, M.K., Kamal Kalaitzidis, Stavros P Abdullah, Shorish Mustafa, *Newly discovered gossanite-like and sulfide ore bodies associated with microbial activity in the zagros ophiolites from the rayat area of ne iraq.* Ore Geology Reviews, 2021. **135**: p. 104191.
10. Etabi, W., *Iron ore deposit&occurrences of iraq.* 1982.
11. Al-Bassam, K., *Final report on the regional geological survey of iraq. Vol. 5 economic geology of iraq.* 1984.
12. Alavi, M., *Tectonics of the zagros orogenic belt of iran: New data and*

interpretations. Tectonophysics, 1994. **229**(3-4): p. 211-238.
13. Alavi, M., *Regional stratigraphy of the zagros fold-thrust belt of iran and its proforeland evolution.* American journal of Science, 2004. **304**(1): p. 1-20.
14. Othman, A.A. and R. Gloaguen, *Automatic extraction and size distribution of landslides in kurdistan region, ne iraq.* Remote Sensing, 2013. **5**(5): p. 2389-2410.
15. Pirouei, M., K. Kolo, and S.P. Kalaitzidis, *Hydrothermal listvenitization and associated mineralizations in zagros ophiolites: Implications for mineral exploration in iraqi kurdistan.* Journal of Geochemical Exploration, 2020b. **208**: p. 106404.
16. Moores, E.M., L.H. Kellogg, and Y. Dilek, *Tethyan ophiolites, mantle convection, and tectonic" historical contingency": A resolution of the" ophiolite conundrum".* SPECIAL PAPERS-GEOLOGICAL SOCIETY OF AMERICA, 2000: p. 3-12.
17. Sissakian, V., *Geological map of iraq (1: 1000000) sheet no. 1.* 2000, GEOSURV, Baghdad.
18. McDonough, W.F. and S.-S. Sun, *The composition of the earth.* Chemical geology, 1995. **120**(3-4): p. 223-253.
19. Rudnick, R. and S. Gao, *Composition of the continental crust in treatise on geochemistry editors-in-chief: Heinrich holland and karl turekian.* 2014.
20. McKenzie, R., *The adsorption of lead and other heavy metals on oxides of manganese and iron.* Soil Research, 1980. **18**(1): p. 61-73.
21. Ayupova, N. and V. Maslennikov. *Biomineralization in ferruginous-siliceous sediments of massive sulfide deposits of the urals*. in *Doklady Earth Sciences*. 2012. Springer Nature BV.
22. Hollis, S.P., et al., *Distribution, mineralogy and geochemistry of silica-iron exhalites and related rocks from the tyrone igneous complex: Implications for vms mineralization in northern ireland.* Journal of Geochemical Exploration, 2015. **159**: p. 148-168.
23. Eggleton, R.A., *Regolith mineralogy*. Regolith Science. CSIRO Publishing, Australia, 2009: p. 45-72.
24. Krajewski, K.P., et al., *Biological processes and apatite formation in sedimentary environments.* Eclogae Geologicae Helvetiae, 1994. **87**(3): p. 701-746.
25. Wood, S.A., *The aqueous geochemistry of the rare-earth elements and yttrium: 2. Theoretical predictions of speciation in hydrothermal solutions to 350 c at saturation water vapor pressure.* Chemical Geology, 1990. **88**(1-2): p. 99-125.
26. Afify, A., M.E. Sanz-Montero, and J. Calvo, *Differentiation of ironstone types by using rare earth elements and yttrium geochemistry–a case study from the bahariya region, egypt.* Ore Geology Reviews, 2018. **96**: p. 247-261.
27. Wei, S., et al., *Geochemical characteristics of rare earth elements in the chaluo hot springs in western sichuan province, china.* Frontiers in Earth Science, 2022: p. 425.
28. Russell, M., M. Solomon, and J. Walshe, *The genesis of sediment-hosted, exhalative zinc+ lead deposits.* Mineralium Deposita, 1981. **16**(1): p. 113-127.
29. Loberg, B.E. and A.-K. Horndahl, *Ferride geochemistry of swedish precambrian iron ores.* Mineralium deposita, 1983. **18**(3): p. 487-504.
30. Bajwah, Z., P. Seccombe, and R. Offler, *Trace element distribution, co: Ni ratios and genesis of the big*

cadia iron-copper deposit, new south wales, australia. Mineralium Deposita, 1987. **22**(4): p. 292-300.
31. Wu, T., et al., *Origin and enrichment of vanadium in the lower cambrian black shales, south china.* ACS omega, 2021. **6**(41): p. 26870-26879.
32. Zhang, J., et al., *Microbial reduction and precipitation of vanadium by mesophilic and thermophilic methanogens.* Chemical Geology, 2014. **370**: p. 29-39.
33. Breit, G.N. and R.B. Wanty, *Vanadium accumulation in carbonaceous rocks: A review of geochemical controls during deposition and diagenesis.* Chemical Geology, 1991. **91**(2): p. 83-97.
34. Awan, R.S., et al., *The occurrence of vanadium in nature: Its biogeochemical cycling and relationship with organic matter—a case study of the early cambrian black rocks of the niutitang formation, western hunan, china.* Acta Geochimica, 2021. **40**(6): p. 973-997.
35. Premović, P.I., M.S. Pavlović, and N.a.Z. Pavlović, *Vanadium in ancient sedimentary rocks of marine origin.* Geochimica et Cosmochimica Acta, 1986. **50**(9): p. 1923-1931.
36. Magnusson, N.H., *Magnusson, nh mellersta och södra sverige*. Vol. 1. 1973: Almqvist & Wiksell.
37. Chi Fru, E.K., Stephanos Ivarsson, Magnus Rattray, Jayne E Gkika, Katerina McDonald, Iain He, Qian Broman, Curt, *Sedimentary mechanisms of a modern banded iron formation on milos island, greece.* Solid Earth, 2018. **9**(3): p. 573-598.
38. Posth, N.R., K.O. Konhauser, and A. Kappler, *Microbiological processes in banded iron formation deposition.* Sedimentology, 2013. **60**(7): p. 1733-1754.
39. Pirouei, M., K. Kolo, and S.P. Kalaitzidis, *Chromium-rich muscovite mineralization in zagros ophiolites in iraqi kurdistan: A study on fuchsite paragenetic association with listvenite types.* Arabian Journal of Geosciences, 2020a. **13**(17): p. 1-13.
40. Aswad, K.J., N.R. Aziz, and H.A. Koyi, *Cr-spinel compositions in serpentinites and their implications for the petrotectonic history of the zagros suture zone, kurdistan region, iraq.* Geological magazine, 2011. **148**(5-6): p. 802-818.
41. Mohammad, Y.O., *Serpentinites and their tectonic signature along the northwest zagros thrust zone, kurdistan region, iraq.* Arabian Journal of Geosciences, 2011. **4**(1): p. 69-83.
42. Aziz, N.R., K.J. Aswad, and H.A. Koyi, *Contrasting settings of serpentinite bodies in the northwestern zagros suture zone, kurdistan region, iraq.* Geological Magazine, 2011. **148**(5-6): p. 819-837.